

ARTICLE

CNS-localized myeloid cells capture living invading T cells during neuroinflammation

Beatrice Wasser^{1*}, Dirk Luchtman^{1*}, Julian Löffel¹, Kerstin Robohm¹, Katharina Birkner¹, Albrecht Strohm², Christina Francisca Vogelaar¹, Frauke Zipp^{1**}, and Stefan Bittner^{1**}

To study the role of myeloid cells in the central nervous system (CNS) in the pathogenesis of multiple sclerosis (MS) and its animal model, experimental autoimmune encephalomyelitis (EAE), we used intravital microscopy, assessing local cellular interactions in vivo in EAE animals and ex vivo in organotypic hippocampal slice cultures. We discovered that myeloid cells actively engulf invading living Th17 lymphocytes, a process mediated by expression of activation-dependent lectin and its T cell-binding partner, N-acetyl-D-glucosamine (GlcNAc). Stable engulfment resulted in the death of the engulfed cells, and, remarkably, enhancement of GlcNAc exposure on T cells in the CNS ameliorated clinical EAE symptoms. These findings demonstrate the ability of myeloid cells to directly react to pathogenic T cell infiltration by engulfing living T cells. Amelioration of EAE via GlcNAc treatment suggests a novel first-defense pathway of myeloid cells as an initial response to CNS invasion and demonstrates that T cell engulfment by myeloid cells can be therapeutically exploited in vivo.

Introduction

Variable roles of resident myeloid cells of the brain have been reported in both the healthy and diseased state (Giles et al., 2018; Schafer and Stevens, 2015; Shemer et al., 2015). Aside from defending against invading pathogens, they also use their phagocytic capacity to clear cellular debris, infectious agents, or neurons undergoing programmed cell death, thereby attempting to maintain tissue homeostasis. In steady state, myeloid cells actively scan their environment by prolonging and retracting their highly motile processes in order to screen the central nervous system (CNS) tissue with a turnover of just a few hours (Nimmerjahn et al., 2005).

In experimental autoimmune encephalomyelitis (EAE), an animal model mimicking many aspects of the neuroinflammatory disease multiple sclerosis (MS), in vivo experiments support a detrimental role of myeloid cells (Heppner et al., 2005). Inhibition of myeloid cell function repressed clinical EAE severity in a bone marrow chimera model and reduced both axonal destruction (Heppner et al., 2005) and secretion of proinflammatory cytokines and chemokines in the spinal cord (Goldmann et al., 2013). However, myeloid cell function was also reported to change properties context dependently in the course of the disease (Giles et al., 2018). In contrast to their well-characterized neurotoxic ability, a potential neuroprotective function of CNS myeloid cells

is far less understood (Kerschensteiner et al., 2003). Studies investigating polarized “anti-inflammatory” microglia that are able to secrete anti-inflammatory cytokines such as IL-10 were usually performed under in vitro conditions (Lobo-Silva et al., 2017; Napoli and Neumann, 2010). A beneficial in vivo function of myeloid cells of the CNS was found in cuprizone models, in which effective clearance of myelin debris by myeloid cells was demonstrated (Lampron et al., 2015; Olah et al., 2012; Sierra et al., 2013). Live interaction between myeloid cells of the brain and CNS-infiltrating immune cells in vivo has not been investigated up to now.

Here, we applied intravital two-photon laser scanning microscopy to unravel physiologically meaningful myeloid cell responses in the CNS in vivo. In particular, we were interested in responses to the infiltration of nonresident activated T helper 17 (Th17) cells into the CNS using EAE as a disease model (Aktas et al., 2005; Paterka et al., 2016; Siffrin et al., 2010). CNS myeloid cells and Th17 cells interacted frequently and intensely during the initial phase of the disease, underlining a dynamic cell communication system in inflammatory lesions. Unexpectedly, myeloid cells were able to engulf viable and motile T cells in the CNS, a phenomenon that occurred more frequently after inflammatory myeloid cell activation and was regulated by lectin

¹Department of Neurology, Focus Program Translational Neuroscience and Immunotherapy, Rhine Main Neuroscience Network, University Medical Center of the Johannes Gutenberg University Mainz, Mainz, Germany; ²Focus Program Translational Neurosciences, Institute for Microscopic Anatomy and Neurobiology, Johannes Gutenberg University Mainz, Mainz, Germany.

*B. Wasser and D. Luchtman contributed equally to this paper; **F. Zipp and S. Bittner contributed equally to this paper; Correspondence to Frauke Zipp: zipp@uni-mainz.de; Stefan Bittner: bittner@uni-mainz.de.

© 2020 Wasser et al. This article is distributed under the terms of an Attribution–Noncommercial–Share Alike–No Mirror Sites license for the first six months after the publication date (see <http://www.rupress.org/terms/>). After six months it is available under a Creative Commons License (Attribution–Noncommercial–Share Alike 4.0 International license, as described at <https://creativecommons.org/licenses/by-nc-sa/4.0/>).

expression on myeloid cells and T cell activity-dependent N-acetyl-D-glucosamine (GlcNAc) exposure. This engulfment led to subsequent cell death in the majority of the engulfed T cells, and EAE was ameliorated when this pathway was enhanced by intrathecal GlcNAc administration.

Results

CX3CR1⁺ cells engulf invading and pathogenic Th17 cells in EAE

To analyze how CX3CR1⁺ myeloid cells (microglia and infiltrating macrophages/dendritic cells) react toward a T cell-driven CNS inflammation, we visualized the dynamic interactions of both cell types using in vivo two-photon laser scanning microscopy in the upper brainstem, an area prone to active inflammation in EAE (Siffrin et al., 2010, 2015). For this purpose, we induced EAE by transfer of fluorescent MOG_{35–55} peptide-specific Th17-skewed cells (2D2-RFP or 2D2-CFP) into recipient mice, in which the expression of GFP is driven by the CX3CR1 promoter (CX3CR1^{GFP}), thus allowing the visualization of CX3CR1⁺ cells and T cells. In the CNS of EAE-diseased mice, infiltrating pathogenic T cells were found to intensely interact with CX3CR1^{GFP} cells, revealing multiple types of interactions. Remarkably, in-depth analyses of the surface-reconstructed images demonstrated the capability of CX3CR1⁺ cells to fully engulf CNS-infiltrating pathogenic Th17 cells (Fig. 1, A–D; and Video 1). The engulfed T cells either stayed engulfed for up to several hours or were able to escape this engulfment. These observations thus suggest an active, albeit not completely successful attempt of the CNS-resident CX3CR1⁺ myeloid cells to remove invading T cells in the inflamed CNS.

CNS-resident myeloid cells are responsible for engulfment processes in organotypic slice cultures

In vivo, peripheral CX3CR1^{GFP} myeloid cells are able to infiltrate the CNS under EAE conditions (Ajami et al., 2018; Geissmann et al., 2003; Goldmann et al., 2013; Jung et al., 2000) and may thus contribute to the observed interactions between CX3CR1^{GFP} myeloid cells and T cells. Using organotypic hippocampal slice cultures prepared from CX3CR1^{GFP} mice co-cultured with pathogenic T cells allowed us to predominantly focus on microglia–T cell interactions, while we cannot formally exclude a low contribution of other myeloid cell types. In these cultures, we confirmed that resident myeloid cells in the CNS readily engaged and engulfed T cells, similar to what we witnessed in vivo (Fig. 2 A and Video 2). To classify all observed interactions, we distinguished five different types of myeloid cell–T cell interactions, based on the in vivo and ex vivo observations (Fig. 2 A). Besides expected “temporary” (defined as contact lasting <10 min of continuous contact; Video 3) and “stable” (≥10 min of continuous contact; Video 4) contacts, we found three types of previously undescribed engulfment-related processes: full and stable engulfment of T cells (shortly termed “engulfment”; Video 5), unstable engulfment followed by T cell migration through the myeloid cell cytoplasm and escape (shortly termed “escapes”; Video 6), and active prolongation of myeloid cell extensions toward and around T cells, successful or not (“engulfment attempts”; Video 7). All these engulfment-related interactions

(engulfment, escape, and engulfment attempt) were grouped under the term “engulfment processes” (EPs; Fig. 2 A). Immunohistochemistry was performed in addition to confirm the observation of the engulfment of CD4⁺ T cells (Fig. 2 B).

Engulfed living T cells either escape or undergo cell death

To determine the viability of engulfed T cells, we stained for Caspase-3/7 activity before live two-photon imaging, allowing the distinction between viable and apoptotic cells. We found that living T cells (CFP-positive), early apoptotic T cells (low Caspase-3/7 expression and diminished CFP-reporter signal), and apoptotic T cells became engulfed by myeloid cells (Fig. 3 A). Long-term imaging of stably engulfed T cells typically showed a gradual reduction of the CFP fluorescence signal, indicating the degradation of these T cells and their genetically encoded reporter signal (CFP) within myeloid cells (Fig. 3 B and Video 8). By contrast, escaping T cells did not lose their fluorescence signal, and their viability was indicated by an active migration in the tissue after escape (Fig. 3 C and Video 9). Escaped T cells showed comparable T cell motilities before and after engulfment, suggesting an unchanged activation status (Fig. 3 D). Importantly, the percentage of stably engulfed T cells was significantly higher compared with the percentage of T cells that were able to escape from engulfment (Fig. 3 E).

Engulfment of viable cells is not dependent on PS exposure

As a reversible expression of “eat-me” signals (such as phosphatidylserine [PS]) on stressed (but otherwise viable) cells might already lead to recognition by phagocytic cells (Brown and Neher, 2014), we analyzed the PS expression of Th17 cells and indeed identified a higher PS expression on activated Th17 cells compared with nonactivated Th17 cells (Fig. 4 A). Consistent with the known phagocytic abilities of CNS myeloid cells (Sierra et al., 2013), we observed Caspase-3/7⁺ cells to be more frequently engulfed by myeloid cells than viable T cells (Fig. 4, B and F). Nonetheless, a detailed quantification showed that the EP frequency of viable T cells was as high as 13% of all interactions between living non-Caspase-3/7⁺ T cells and myeloid cells (Fig. 4 C). Treatment with high concentrations of soluble Annexin V, in order to mask PS signals (Lu et al., 2011), significantly reduced both the total EPs and the engulfment rate of apoptotic cells but had no effect on EPs and engulfment rate of living T cells (Fig. 4, D–F). Annexin V treatment also did not impact T cell motility parameters (Fig. 4 G). These data suggest that despite PS expression on living Th17 cells, the engulfment of viable T cells is mediated by a PS-independent mechanism, in contrast to the PS-dependent phagocytosis of apoptotic cells.

Engulfment of viable cells is dependent on GlcNAc exposure on activated T cells

To identify the receptor on T cells responsible for the engulfment of living cells, we analyzed other eat-me and “don’t eat-me” signals. Of note, expression of the don’t eat-me signal CD47 was not detected on Th17 cells (data not shown). Furthermore, the recognition of eat-me signals via vitronectin receptors has been discussed to promote the phagocytosis of apoptotic cells (Savill, 1997). We observed no influence on the engulfment of

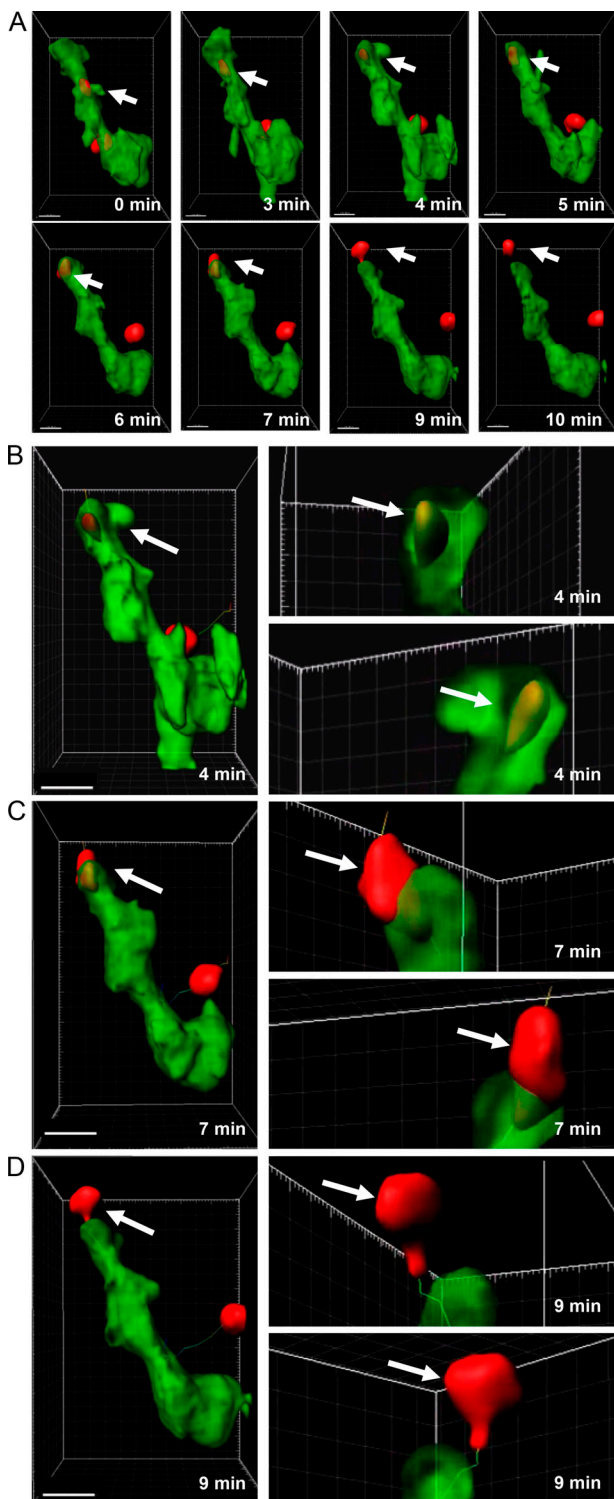


Figure 1. Viable T cells in EAE lesions can be engulfed *in vivo* by CX3CR1^{GFP} cells without subsequent cell death. EAE was induced in CX3CR1^{GFP} (green) mice or CX3CR1.GFPxRag mice via the passive transfer of B6.2D2.RFP.Th17 cells (red). At the peak of disease, ~11 d after immunization, interactions were imaged *in vivo* with intravital two-photon imaging ($n = 12$ mice from three different experiments). **(A)** Time-lapse surface analysis of a representative full engulfment (minutes 3 and 4) of a red fluorescent Th17 cell by a green myeloid cell, followed by the escape from this engulfment (minutes 5–10). Scale bars = 10 μm . **(B–D)** Magnified and 3D-rotated surface analysis of the sequence from **(B)** full engulfment and **(C)** escape to **(D)** full T cell detachment. Scale bars = 15 μm . Arrows point to an escaping T cell.

living cells, as inhibition of this pathway by treatment with the tetrapeptide RGDS (Arg-Gly-Asp-Ser) did not reduce the percentages of engulfment (Fig. 5 A). By contrast, GlcNAc, which has been discussed previously to promote the binding of apoptotic thymocytes to macrophages (Duvall et al., 1985), had a significant impact on T cell-myeloid cell interaction (Fig. 5, B–G). To identify GlcNAc expression on T cells, we used fluorescently labeled wheat germ agglutinin (WGA), which has been used to measure GlcNAc levels (Notter and Leary, 1987). Stimulated Th17 cells showed an increased binding of WGA compared with unstimulated cells and the presence of soluble GlcNAc in the staining solution could interfere with the binding of WGA, leading to lower fluorescence (Fig. 5 B). Using different experimental protocols, addition of soluble GlcNAc can be used either to competitively inhibit endogenous GlcNAc-lectin interaction or to enhance GlcNAc exposure on T cells. Importantly, the competitive addition of 20 mM GlcNAc in the 24 h co-culture of organotypic hippocampal slices with Th17 cells significantly decreased the engulfment of T cells by myeloid cells (Fig. 5, C and D). On the other hand, pretreatment of T cells with 20 mM GlcNAc increased GlcNAc exposure on activated T cells (Fig. 5 E). Increased GlcNAc exposure was stable for up to 5 h in co-cultures with organotypic hippocampal slices (Fig. 5 F). This enhanced GlcNAc exposure on T cells increased EPs and showed a strong trend toward more stable engulfments of viable T cells (Fig. 5, G and H). Engulfment of dying cells showed only a minor trend toward higher engulfment after GlcNAc pretreatment (Fig. S1 A).

Of note, myelin oligodendrocyte glycoprotein (MOG)-specific Th17 cells showed similar interactions with myeloid cells to MOG-specific Th2 cells, MOG-specific regulatory T (T reg) cells (Fig. 5, I and J), and polyclonal Th17 cells (Fig. 5 K). Furthermore, the presence of supplemented MOG peptide in co-cultures of hippocampal slice cultures with pathogenic Th17 cells in order to enhance antigen presentation processes did not enhance engulfment-related processes (Fig. 5 L). In addition, we analyzed the engulfment of Th17 cells in Th17 reporter mice, which switch from a red to a red and green double-positive phenotype upon IL-17 expression (Fig. 5 M). With this analysis, we were able to confirm that not only IL-17-producing Th17 cells became engulfed. We conclude that engulfment processes are regulated by the state of T cell activity rather than by T cell subtype or antigen specificity.

Since our observations pointed toward a specific role of T cell activation status as a prerequisite for engulfment by myeloid cells, we addressed the role of the PI3K/Akt pathway as a major regulator of T cell activity. Indeed, inhibition of this pathway by Wortmannin reduced WGA binding on activated T cells (Fig. 6 A) and abrogated Th17 cell effector functions, as could be shown by a significantly lower IL-17 expression in unstimulated and stimulated Th17 cells (Fig. 6 B), and down-regulated the expression of activation markers (CD44 and CD25) in stimulated Th17 cells *in vitro* (Fig. 6, C and D). Importantly, PI3K inhibition had no influence on migration properties of Th17 cells in organotypic slices (Fig. 6 E) and had no obvious impact on myeloid cell structure or morphology (Fig. 6 F). Treating the hippocampal slice-T cell co-cultures with Wortmannin, we observed a significantly lower engulfment rate compared with control

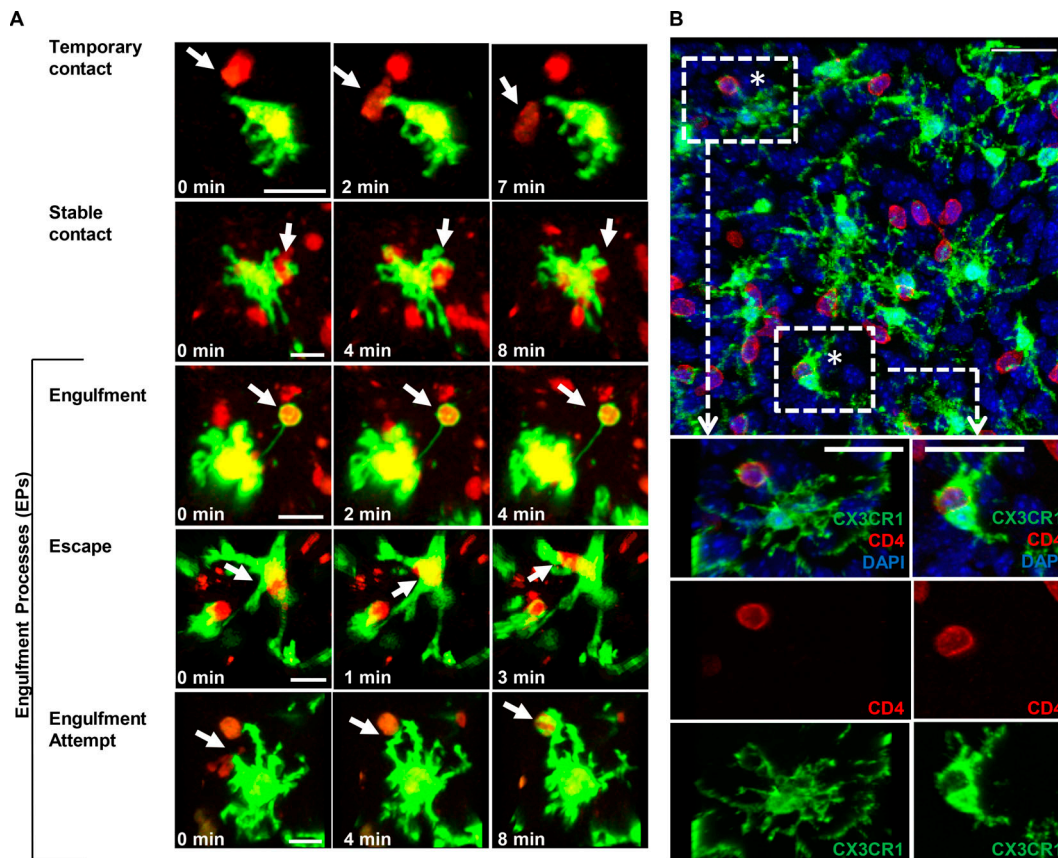


Figure 2. Detailed classification of interactions between myeloid cells and T cells in organotypic hippocampal slice cultures. 24-h co-cultures of organotypic hippocampal slices from CX3CR1^{GFP} pups with pathogenic B6.2D2.RFP.Th17 cells were imaged over a time period of 10 min ($n = 4$ organotypic slices from three different experiments). **(A)** Characterization of all detectable interactions between myeloid cells (green) and T cells (red) ex vivo. Scale bars = 15 μ m. Arrows point to an example of the indicated interaction. **(B)** Immunohistochemical staining of CX3CR1⁺ myeloid cells (anti-GFP, green), CD4⁺ T cells (anti-CD4, red), and cell nucleus (DAPI, blue). Asterisks mark engulfed T cells. Scale bars = 30 μ m. For better visualization, single stainings for two engulfment interactions are shown (right panel).

conditions, indicating an impact of T cell activation status on engulfment probabilities (Fig. 6, F-H). Of note, the activity of T cells not only controls T cell engulfment but might also impact their capacity to escape. While escapes were identified to be low under control conditions (Fig. 3 E), with Wortmannin treatment, there was a nonsignificant trend from stable engulfments to escapes (Fig. 6, I and J).

Amplification of myeloid cell activation enhances engulfment of living T cells

We next aimed to identify the corresponding binding partner on myeloid cells. CD206 has been described previously as a receptor for GlcNAc (Taylor et al., 1992, 2005). Here, we showed that alternative activation of myeloid cells led to a significant up-regulation of lectin expression, which was stronger than the up-regulation of lectin in classically activated myeloid cells (Fig. 7 A). Alternative activation of myeloid cells in the CNS has been described to be important in amelioration of EAE disease (Franco and Fernández-Suárez, 2015; Jiang et al., 2014). Up-regulation of CD206 expression was accompanied by increased engulfment frequencies (Fig. 7 B), indicating that a marked increase in myeloid cell activity supports increased engulfment

processes and thus clearance of invading T cells in neuro-inflammation. Interestingly, CD206 expression was reported in published single-cell RNA-sequencing data to be expressed by microglia-like cells in health and EAE disease (Falcão et al., 2018), and in agreement, we detected a minor fraction of CD45^{lo}CD11b⁺Ly6C/G⁻ myeloid cells expressing CD206 in EAE (Fig. 7, C-E). In addition, we observed CD206 expression in CD45^{hi}CD11b⁺ myeloid cells (Fig. 7, C and E), previously discussed to represent CNS-infiltrating myeloid cells or activated microglia (Ponomarev et al., 2007). Our results emphasize low CD206 expression in EAE conditions in different myeloid cell populations. Of note, these low percentages of CD206 expression (~2-4%) are comparable to percentages of full acute engulfments (Fig. 4 C). We hypothesize a temporary up-regulation of CD206 during the engulfment process. Indeed, we detected CD206 predominantly on T cell-engulfing CX3CR1⁺ cells in the spinal cord of EAE diseased mice (Fig. 7 F). We observed CD206 expression in organotypic slices after alternative activation and in EAE diseased mice not only in perivascular myeloid cells but also in the parenchyma (Fig. S1, B and C). Parenchymal CD206 expression in EAE might be based on either CNS-infiltrating myeloid cells or up-regulation of CD206 by microglia.

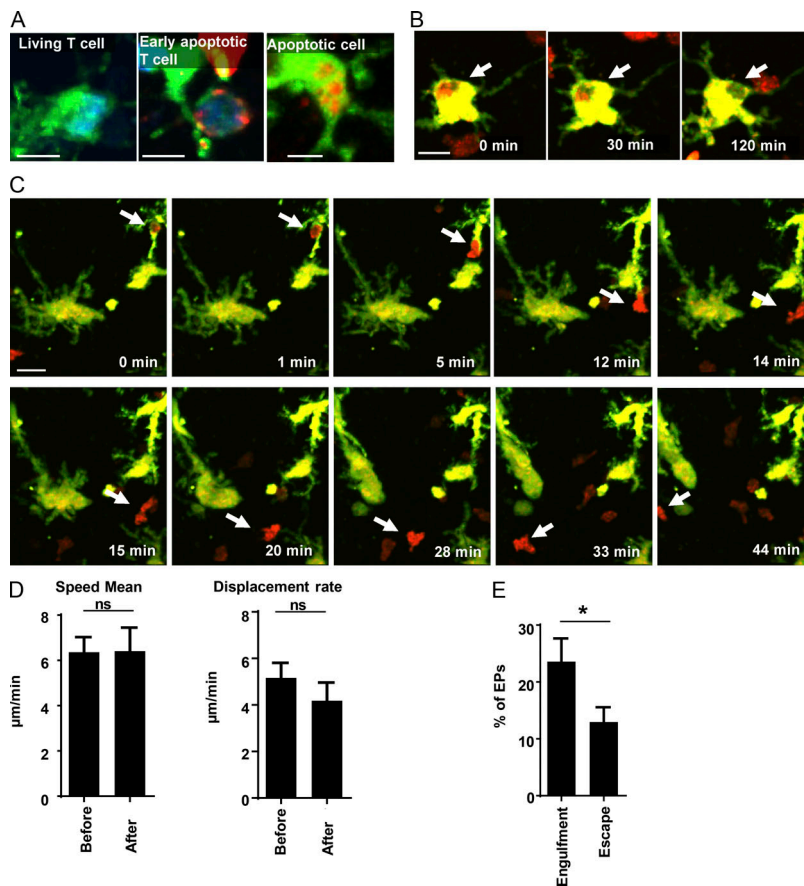


Figure 3. Th17 cell escape from myeloid cells and cell death within myeloid cells after internalization. Co-cultures of hippocampal slices from CX3CR1^{GFP} pups with pathogenic B6.2D2.CFP.Th17 cells were stained with Image-iT LIVE Red Caspase-3 and -7 Detection Kit to identify apoptotic cells. **(A)** Representative identification of viable T cells (blue), early apoptotic T cells (blue and red), and apoptotic/dead cells (red) engulfed by myeloid cells (green) in these co-cultures ($n = 5$ co-cultures from four different experiments). Scale bars = 10 μm . **(B)** Representative sequence of an engulfed Caspase-3/7-negative B6.2D2.CFP Th17 cell (viable, false colored in red for better visualization) imaged over a time period of 120 min via two-photon microscopy ex vivo ($n = 4$ co-cultures from three different experiments). Scale bars = 15 μm . Arrows point to a stably engulfed T cell. **(C)** Representative sequence of an escaped viable T cell (false colored in red for better visualization) for 44 min ex vivo ($n = 4$ co-cultures from three different experiments). Scale bar = 15 μm . Arrows point to an escaping T cell. **(D)** Mean (\pm SEM) T cell motility parameters of viable T cells before ($n = 6$ cells from two different experiments) and after ($n = 6$ cells from two different experiments) the interaction with myeloid cells during the escape process ex vivo. Statistical analysis was performed using two-sided Student's *t* tests. ns, not significant. **(E)** Mean (\pm SEM) percentage of engulfment and escape among the engulfment processes (EPs) ex vivo. $n = 33$ organotypic slices from 20 different experiments. Statistical analysis was performed using two-sided Student's *t* tests. *, $P < 0.05$.

Of note, although engulfment was not dependent on antigen specificity (Fig. 5 K), we did observe that engulfing myeloid cells more frequently showed MHC-II expression compared with nonengulfing myeloid cells (Fig. 7, G and H), confirming that especially active myeloid cells are capable of engulfing T cells.

Engulfment is increased during the initial phase of EAE

To challenge the *in vivo* relevance of our findings, we investigated the relationship between T cell engulfment and EAE disease course. *In vivo*, CNS-invading CD4⁺ T cells during EAE showed higher GlcNAc expression compared with peripheral CD4⁺ T cells, underlining the importance of this pathway for activated T cells in the CNS (Fig. 8 A). Importantly, interaction characteristics between CX3CR1⁺ cells and T cells were not static but depended on clinical disease severity (Fig. 8, B-E; and Video 10). The engulfment of pathogenic T cells was significantly higher in EAE mice exhibiting a clinical score <2 (Fig. 8, B and C). Stable contacts increased in correlation with a higher disease score, while temporary contacts were more abundant at lower disease scores (Fig. 8, B and C). Accordingly, T cell motilities, known to inversely correlate with antigen recognition (Cahalan and Parker, 2008), were altered over the disease score. T cell motility parameters (e.g., “T cell speed” and “T cell displacement rate”) were higher during the early disease course compared with EAE mice exhibiting a clinical score >2 (Fig. 8, D and E). Strikingly, the interactions of CX3CR1⁺ cells and T cells in organotypic hippocampal slice cultures showed overall characteristics comparable to early CNS inflammation *in vivo* (Fig. 8, C-E). The engulfment frequencies of T cells (4%) as well as

the frequencies of stable (20%) and temporary contacts (70–80%) among the interactions were similar *in vivo* and in organotypic hippocampal slice cultures over an observation period of 20 min (Fig. 8 C). Likewise, T cells that invade the CNS in early EAE disease showed T cell motility parameters comparable to T cells invading the hippocampal slices (Fig. 8, D and E). It should be noted that in contrast to this apparently low relative number of T cell engulfments, they can be considered as biologically significant. The percentage of the engulfment of viable cells reflects a snapshot of the processes taking place in the CNS and does not provide the total cell count of removed cells. Altogether, our findings point toward T cell engulfment by CX3CR1⁺ myeloid cells as an early defense mechanism upon initial T cell invasion that is overcome later on in a full-blown inflammatory environment.

Pharmacological increase of the engulfment pathway in mice ameliorates EAE disease severity

As increased GlcNAc expression in T cells correlates with engulfment, we aimed next to therapeutically ameliorate EAE by enhancing GlcNAc exposure on T cells in the CNS *in vivo*. *In vitro*, GlcNAc pretreatment during T cell stimulation was efficient at enhancing GlcNAc exposure on T cells (Fig. 5 D). Upon intrathecal treatment with 1 μmol GlcNAc *in vivo*, we indeed found an amelioration of disease severity (Fig. 8 F). This effect was enhanced when GlcNAc treatment was started before disease onset (Fig. 8 G), confirming a high relevance during the early phase of the disease. Analysis of GlcNAc expression on

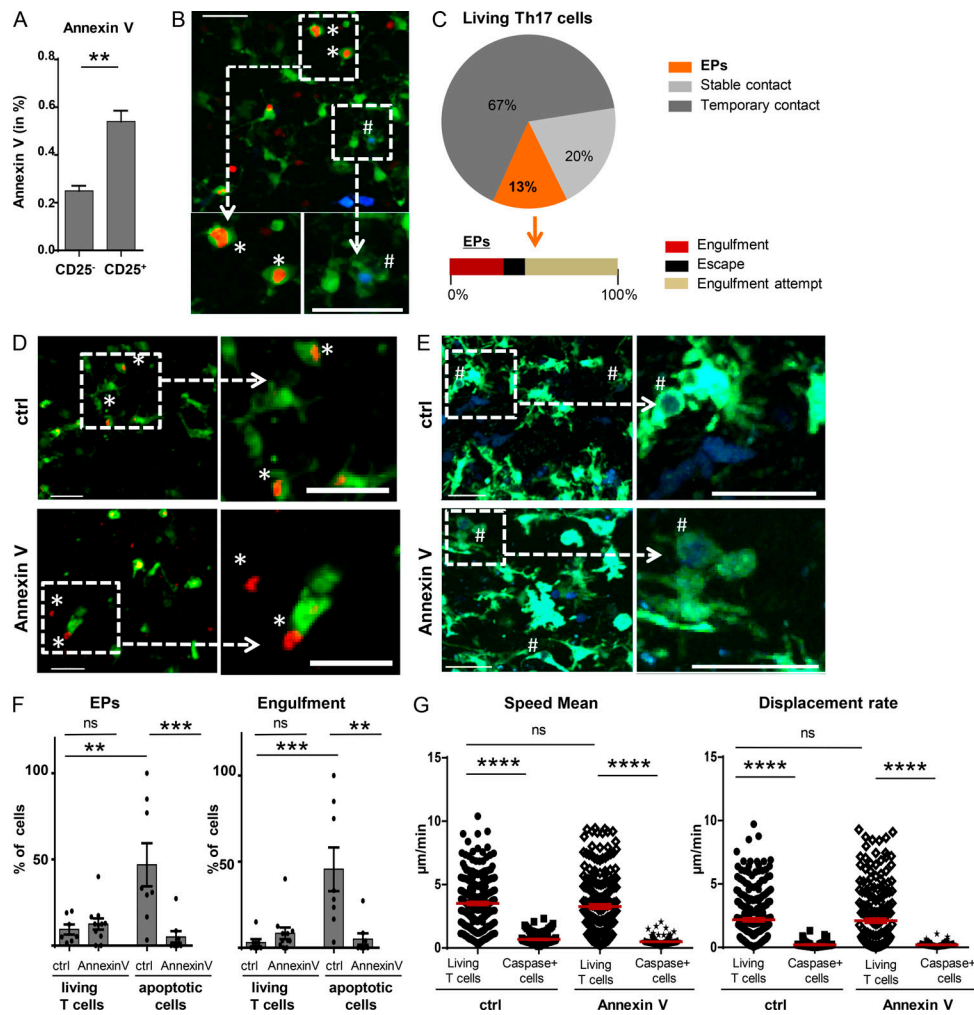


Figure 4. In contrast to phagocytosis, engulfment of living T cells is independent of Annexin V-PS interaction. (A) PS exposure on Th17-skewed cells (day 5 of culture) was determined via Annexin V staining. Mean (± SEM) Annexin V binding was compared between CD25-expressing living CD4⁺ cells and non-CD25-expressing living CD4⁺ cells using flow cytometry analysis ($n = 3$ from two different experiments). (B–G) 24-h co-cultures of organotypic hippocampal slices from CX3CR1^{GFP} pups with pathogenic B6.2D2.CFP.Th17 cells were stained with Image-iT LIVE Red Caspase-3 and Caspase-7 Detection Kit to identify apoptotic cells and imaged over a time period of 20 min with two-photon microscopy. (B) Representative example of the Image-iT LIVE Red Caspase-3 and -7 (red) staining in 24-h co-cultures of organotypic hippocampal slices with B6.2D2.CFP.Th17 cells (blue). Scale bars = 40 μm. Representative of $n = 5$ co-cultures from four different experiments. (C) Pie chart comparing the distribution (%) of interaction modes between myeloid cells and viable 2D2.CFP.Th17 cells ($n = 27$ organotypic slices from 17 different experiments) and contingency bars reflecting the respective distribution of engulfment, escape, and engulfment attempt. (D) Representative two-photon images of the 24-h co-cultures of the organotypic hippocampal slices with B6.2D2.CFP.Th17 cells stained with Image-iT LIVE Red Caspase-3 and -7 Detection Kit, with or without 10 μg/ml Annexin V treatment (24 h). Relevant areas are magnified (right panel); asterisks mark apoptotic cells (red). Scale bars = 40 μm. Representative of $n = 7$ co-cultures from three different experiments. (E) Representative two-photon images of the 24-h co-cultures of the organotypic hippocampal slices with B6.2D2.CFP.Th17 cells stained with Image-iT LIVE Red Caspase-3 and -7 Detection Kit, with or without 10 μg/ml Annexin V treatment (24 h). Relevant areas are magnified (right panel); number signs mark nonapoptotic T cells (blue). Scale bars = 40 μm, representative of $n = 8$ co-cultures from five different experiments. (F) Mean (± SEM) percentages of engagement-related process (EPs; left panel) and full engulfments (right panel) among the detectable cell count (viable T cells and apoptotic cells), without ($n = 7$ organotypic slices for viable cells from five different experiments; $n = 8$ organotypic slices for apoptotic cells from three different experiments) and with Annexin V treatment ($n = 11$ organotypic slices for viable cells from five different experiments, $n = 8$ organotypic slices for apoptotic cells from three different experiments). (G) Mean (± SEM) T cell motility parameters compared between Caspase-3/7⁺ and viable B6.2D2.CFP.Th17 cells without ($n = 10$ organotypic slices, 276 T cells for viable cells from five different experiments; $n = 8$ organotypic slices, 185 T cells for apoptotic cells from three different experiments) and with ($n = 12$ organotypic slices, 205 T cells for viable cells from five different experiments; $n = 8$ organotypic slices, 171 T cells for apoptotic cells from three different experiments) Annexin V treatment. Statistical analysis for A was performed using two-sided Student's *t* tests. Statistical analyses for F and G were performed using one-way ANOVA with Tukey's post hoc test. **, $P < 0.01$; ***, $P < 0.001$; ****, $P < 0.0001$; ns, not significant.

T cells isolated from treated mice confirmed a higher expression of GlcNAc on T cells compared with the control group (Fig. 8 H). By contrast, intrathecal GlcNAc treatment had no effect on GlcNAc exposure on peripheral T cells (Fig. 8 H). Thus, GlcNAc treatment specifically affected T cells, which infiltrated into the

CNS, excluding peripheral immune effects and demonstrates that T cell engulfment by myeloid cells can be therapeutically exploited in vivo. GlcNAc treatment significantly reduced the T cell count within the CNS, indicating a removal of T cells by engulfing myeloid cells (Fig. 8, I and J).

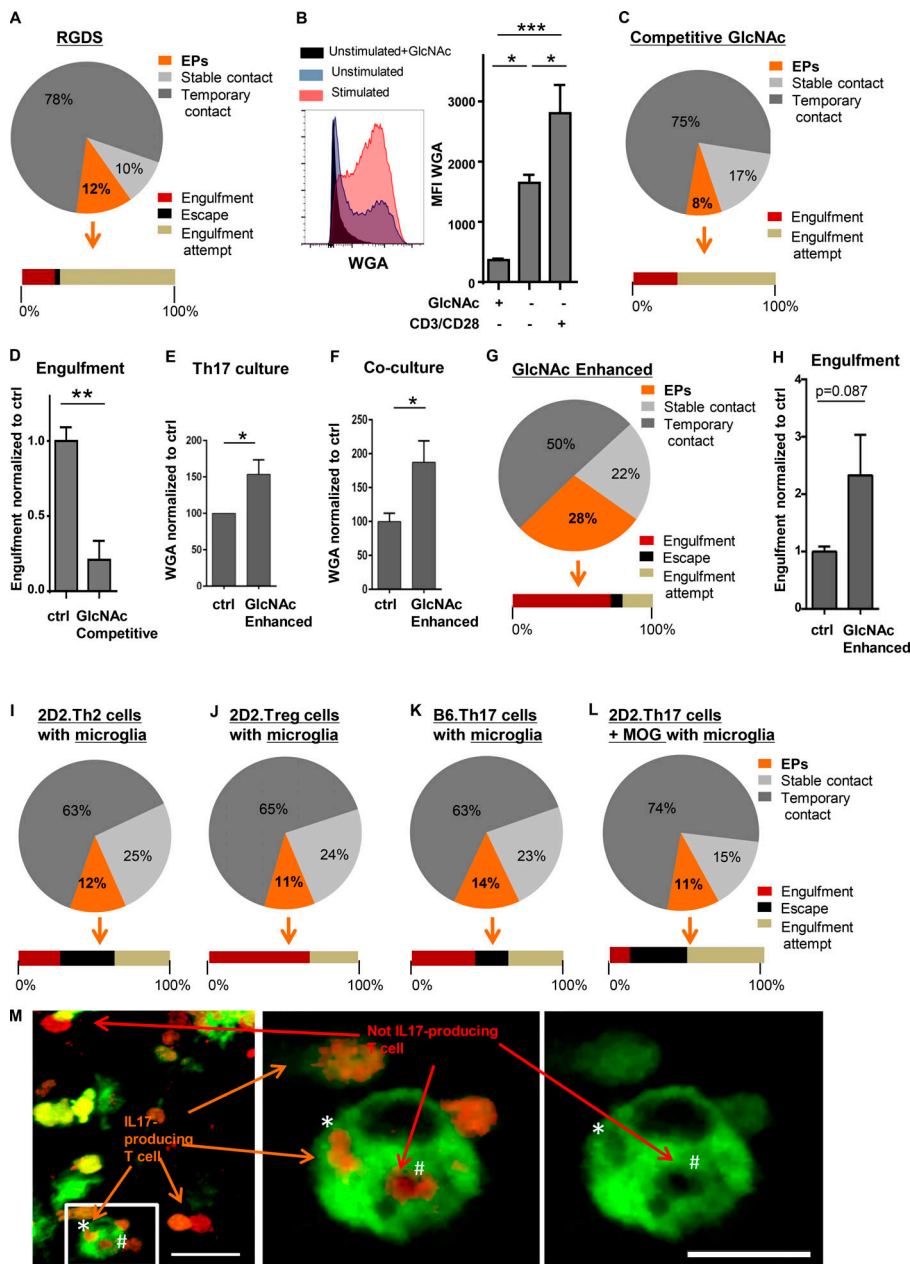


Figure 5. Engulfment of viable cells is dependent on GlcNAc exposure on activated T cells. (A, C, D, and G–L) Co-cultures of organotypic hippocampal slices from CX3CR1^{GFP} pups with pathogenic CFP-labeled T cells were stained with Image-iT LIVE Red Caspase-3 and -7 Detection Kit to identify apoptotic cells and imaged over a time period of 20 min. Only non-apoptotic T cells were considered for further analyses. **(A)** 24-h co-cultures of organotypic hippocampal slices with Th17 cells were treated with RGDS (1 mM). The pie chart comparing the distribution (%) of interaction modes between myeloid cells and viable B6.2D2.CFP.Th17 cells ($n = 5$ organotypic slices from four different experiments) and contingency bar reflecting the respective distribution of engulfment, escape, and engulfment attempt are shown. **(B)** WGA binding to Th17-skewed cells was assessed in the presence or absence of GlcNAc (200 mM) in the staining solution using flow cytometric analysis. Representative histograms (left panel) and mean (\pm SEM) of the mean fluorescence intensity (MFI, right panel) are shown ($n = 5$ Th17 cultures from two different experiments). **(C)** 24-h co-cultures of organotypic hippocampal slices with Th17 cells were treated with GlcNAc (20 mM, competitive GlcNAc). The pie chart shows the distribution (%) of interaction modes between myeloid cells and viable Th17 cells ($n = 4$ organotypic slices from three different experiments; upper panel), and contingency bar reflects the respective distribution of engulfment and engulfment attempt (lower panel). **(D)** Mean (\pm SEM) percentages of engulfment rate among the interactions in GlcNAc (20 mM) treated co-cultures ($n = 4$ organotypic slices from three different experiments) normalized to the untreated control group ($n = 4$ organotypic slices from 3 different experiments). **(E–H)** Naive T cells were skewed into Th17 cells in the presence or absence of GlcNAc (20 mM). At day 3 of culture, cells were further stimulated with antiCD3 and antiCD28 with/without GlcNAc (20 mM). **(E)** Cells were washed to remove GlcNAc in the supernatant, and WGA binding was assessed ($n = 7$ Th17 cell cultures from seven different experiments). **(F–H)** Control Th17-skewed cells and GlcNAc-pretreated (GlcNAc enhanced) Th17-skewed cells were co-cultured with organotypic hippocampal slices. **(F)** WGA-binding to T cells was assessed after 5h of co-culture ($n = 7$ Th17 co-cultures from three different experiments). **(G)** The pie chart shows the distribution (%) of interaction modes between myeloid cells and viable GlcNAc-pretreated Th17 cells ($n = 7$ organotypic slices from three different experiments; upper panel), and contingency bar reflects the respective distribution of engulfments and engulfment attempts (lower panel). **(H)** Mean (\pm SEM) percentages of engulfment rate among the interactions of GlcNAc-pretreated Th17-skewed cells in organotypic hippocampal slices ($n = 7$ organotypic slices from three different experiments) normalized to the GlcNAc-untreated control group ($n = 7$ organotypic slices from three different experiments). **(I–L)** Pie charts (upper panel) show the distribution (%) of interaction modes between myeloid cells and viable B6.2D2.CFP.Th2 cells ($n = 3$ organotypic slices from three different experiments; I), viable B6.2D2.CFP.T reg cells ($n = 4$ organotypic slices from four different experiments; J), polyclonal B6.CFP.Th17 cells (Th17 BL/6; $n = 6$ organotypic slices from 2 different experiments; K), or viable B6.2D2.CFP.Th17 cells in co-cultures treated with MOG (100 μ g/ml; $n = 3$ organotypic slices from two different experiments; L), and contingency bars reflect the respective distribution of engulfment, escape, and attempt to engulf (lower panel). **(M)** Representative visualization of 24-h co-cultures of organotypic hippocampal slices from CX3CR1^{GFP} pups with pathogenic B6.2D2.RFP.Th17.GFP reporter cells, in which IL-17-producing cells are RFP⁺GFP⁺ double positive (orange), while non-IL-17-producing cells are RFP⁺ single positive (red; representative of $n = 3$ co-cultures from three different experiments; left panel). Scale bar = 30 μ m. A myeloid cell (green) engulfing at the same time an IL-17-producing cell (marked with an asterisk) and a non-IL-17-producing cell (marked with a number sign) was magnified (middle panel), and red signal was hidden to visualize the green signal of the IL-17-producing T cell (right panel). Scale bar = 15 μ m. Statistical analyses were performed using two-sided Student's *t* tests. *, $P < 0.05$; **, $P < 0.01$; ***, $P < 0.001$; ns, not significant.

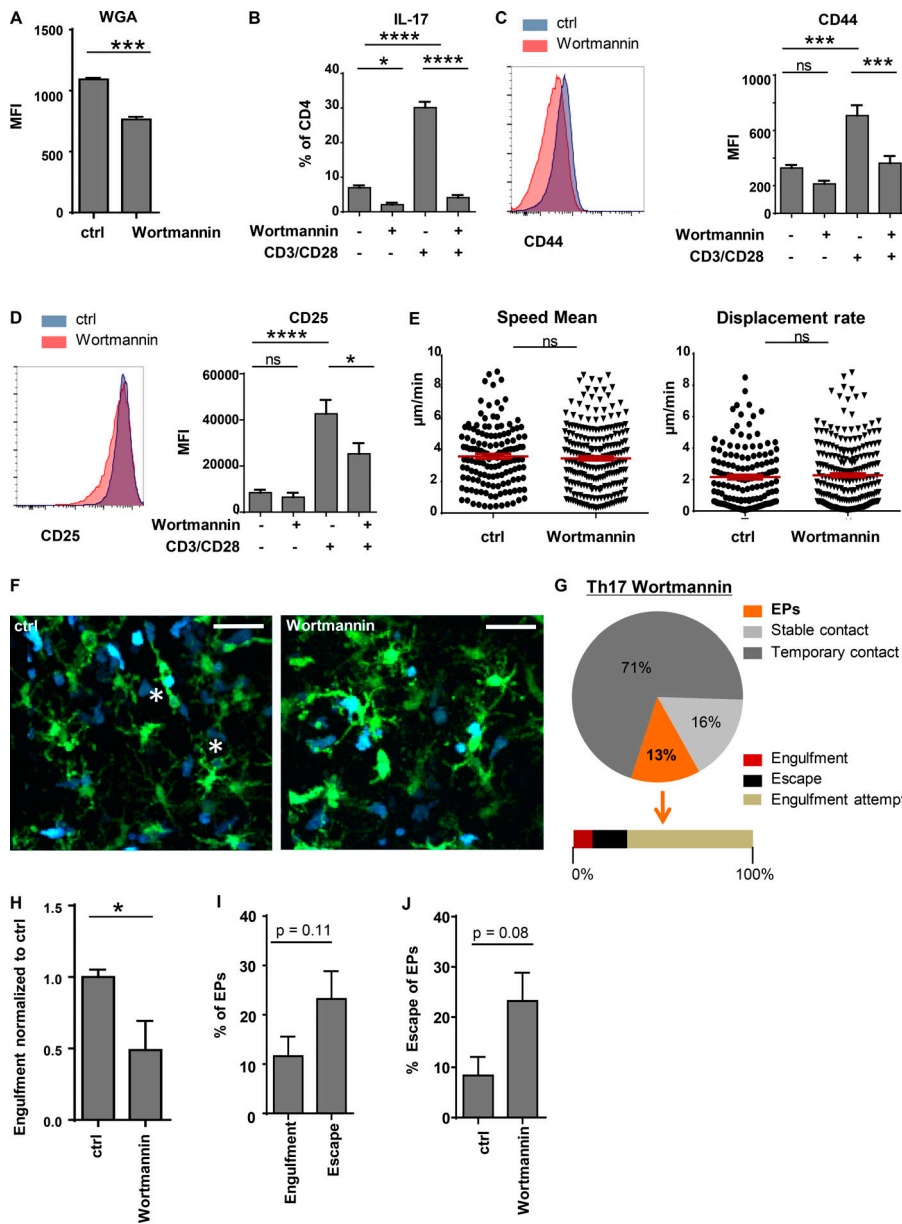


Figure 6. Modulation of T cell activity alters T cell engulfment. (A–D) Th17-skewed cells (day 5 of culture) were either stimulated for 24 h with anti-CD3 and anti-CD28 or not, with or without Wortmannin. (A) Quantification of the mean fluorescence intensity (MFI) of WGA binding on stimulated, living CD4⁺ T cells with or without Wortmannin (*n* = 3 from two different experiments). (B) Brefeldin A was added to the T cells 4 h before the analysis in order to inhibit secretion of IL-17. Quantification of IL-17 expression among CD4⁺ T cells (mean ± SEM; *n* = 6 from two different experiments). (C) Histogram and quantification (mean ± SEM) of CD44 expression among living CD4⁺ T cells (*n* = 6 from two different experiments). (D) Histogram and quantification (mean ± SEM) of CD25 expression among living CD4⁺ T cells (*n* = 6 from two different experiments). (E–J) 24-h co-cultures of organotypic hippocampal slices with Th17 cells were treated with Wortmannin. (E) T cell motility parameters of viable B6.2D2.CFP.Th17 cells without (*n* = 5 organotypic slices, 141 T cells from four different experiments) and with (*n* = 8 organotypic slices, 228 T cells from four different experiments) Wortmannin treatment (2.5–5 µM; mean ± SEM). (F) Representative images of organotypic hippocampal slices with pathogenic B6.2D2.CFP.Th17 cells with (*n* = 8 organotypic slices from four different experiments) and without (*n* = 5 organotypic slices from four different experiments) Wortmannin (2.5–5 µM) treatment. Asterisks mark engulfed T cells. Scale bars = 40 µm. (G) Pie chart showing the distribution (%) of interaction modes between myeloid cells and viable T cells in Wortmannin (2.5–5 µM)-treated co-cultures of organotypic hippocampal slices with B6.2D2.CFP.Th17 cells (*n* = 8 organotypic slices from four different experiments; upper panel) and contingency bars reflecting the respective distribution of engulfment, escape, and attempt to engulf (lower panel). (H) Mean (± SEM) percentages of engulfment rate among the interactions in Wortmannin (2.5–5 µM)-treated organotypic hippocampal slices (*n* = 8 organotypic slices from four different experiments) normalized to

the untreated control group (*n* = 5 organotypic slices from four different experiments). (I) 24-h co-cultures of Wortmannin-treated organotypic hippocampal slices from CX3CR1^{GFP} pups with pathogenic B6.2D2.CFP.Th17 cells were stained with Image-iT LIVE Red Caspase-3 and -7 Detection Kit to identify apoptotic cells and imaged over a time period of 20 min. Only nonapoptotic T cells were considered for further analyses. Engulfment and escape frequencies were determined among EPs (*n* = 8 from four different experiments). (J) 24-h co-cultures of Wortmannin-treated or untreated organotypic hippocampal slices from CX3CR1^{GFP} pups with pathogenic B6.2D2.CFP.Th17 cells were stained with Image-iT LIVE Red Caspase-3 and -7 Detection Kit to identify apoptotic cells and imaged over a time period of 20 min. Only nonapoptotic T cells were considered for further analyses. Escape frequencies among EPs are shown (*n* = 5 controls, 8 Wortmannin-treatments from four different experiments). Statistical analyses for A, E, and G–J were performed using two-sided Student’s *t* tests. Statistical analyses for B–D were performed using one-way ANOVA with Tukey’s post hoc test. *, *P* < 0.05; **, *P* < 0.01; ***, *P* < 0.001; ****, *P* < 0.001, ns, not significant.

Discussion

Myeloid cell activation in the CNS is a hallmark of inflammatory lesions in EAE and MS, where myeloid cells of the brain continuously scan their environment, mediating both detrimental and tissue homeostatic functions, presumably depending on the context (Giles et al., 2018; Heneka et al., 2014; Jolivel et al., 2015; Nimmerjahn et al., 2005). Although it is well known that pathogenic Th17 cells invade the CNS during MS and EAE, thereby mediating inflammation and neuronal degeneration

(Dendrou et al., 2015; Goverman, 2009), whether they engage resident myeloid cells directly has not been clarified. Using live imaging, we observed CX3CR1⁺ cells and T cells forming cell-in-cell structures in vivo in the CNS upon early neuroinflammation, predominantly resulting in T cell death. These engulfment processes were dependent on both the activity of CX3CR1⁺ myeloid cells and the GlcNAc exposure on activated T cells. Thus, it appears likely that CX3CR1⁺ cells such as microglia attempt to remove CNS-invading living T cells in a

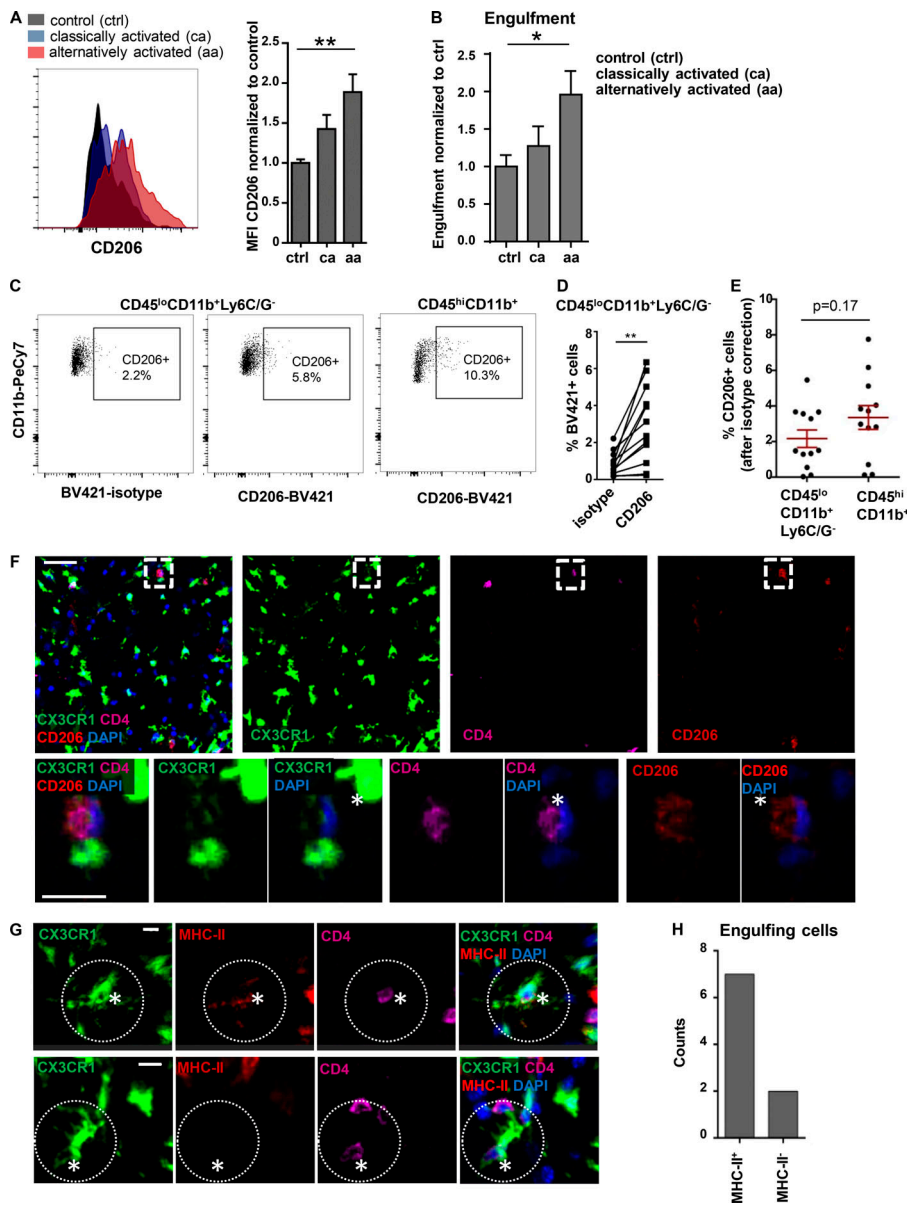


Figure 7. Amplification of myeloid cell activation enhances engulfment of living T cells. **(A)** Flow cytometric analysis of lectin CD206 in living myeloid cells (propidium iodide [PI]-GFP⁺) in organotypic hippocampal slices prepared from CX3CR1^{GFP} pups and treated for 24 h with LPS (1 μg/ml; classical activation) or a combination of LPS (1 μg/ml), dexamethasone (5 × 10⁻⁷ M), and IL-4 (10 ng/ml; alternative activation) in comparison to untreated organotypic hippocampal slices (n = 7 controls from four different experiments, 7 LPS-treated slices from four different experiments, 3 LPS/dexamethasone/IL-4-treated slices from two different experiments). **(B)** 24-h co-cultures of organotypic hippocampal slices from CX3CR1^{GFP} pups with pathogenic B6.2D2.CFP.Th17 cells were stained with Image-iT LIVE Red Caspase-3 and -7 Detection Kit to identify apoptotic cells and imaged over a time period of 20 min. Only nonapoptotic T cells were considered for further analyses. The organotypic slices were stimulated with LPS (1 μg/ml) or a combination of LPS (1 μg/ml), dexamethasone (5 × 10⁻⁷ M), and IL-4 (10 ng/ml) for 24 h in order to activate myeloid cells. Mean (± SEM) percentages of engulfment among the interactions in classically (LPS) or alternatively (LPS/dexamethasone/IL-4) activated organotypic hippocampal slices with B6.2D2.CFP.Th17 cells (n = 13 classically activated organotypic slices from five different experiments and 8 alternatively activated organotypic slices from three different experiments) normalized to the untreated control group (n = 13 organotypic slices from five different experiments). **(C–E)** Flow cytometry was performed to analyze CD206 expression on CD45^{lo}CD11b⁺Ly6C/G⁻ myeloid cells in the CNS of EAE diseased mice. **(C and D)** Representative dot plots of CD206 staining (CD206-BV421) and isotype control (IgG2ak-BV421) of CD45^{lo}CD11b⁺Ly6C/G⁻ myeloid cells and CD206 staining of CD45^{hi}CD11b⁺ myeloid cells (representative of n = 12 EAE diseased mice from three different experiments). **(C)** Quantitative analysis of BV421 staining in CD45^{lo}CD11b⁺Ly6C/G⁻ myeloid cells comparing CD206 staining and isotype control (n = 12 EAE diseased mice from three different experiments; D). **(E)** Quantification (mean ± SEM) of CD206 percentages of CD45^{lo}CD11b⁺Ly6C/G⁻ or CD45^{hi}CD11b⁺ myeloid cells using CD206-BV421 corrected by subtraction of the signal for the corresponding isotype control (IgG2ak-BV421; n = 12 EAE diseased mice from three different experiments). **(F–H)** Immunohistochemistry was performed to analyze CD206 expression and MHC-II expression on T cell-engulfing myeloid cells in the spinal cord of EAE diseased CX3CR1.GFP mice. **(F)** A representative example of a CD206-expressing engulfing CX3CR1⁺ cell is shown. Scale bars = 30 μm (upper panel) and 15 μm (lower panel); representative of n = 4 residues from two different experiments. A slice view of the engulfing cell was magnified (lower panel). **(G)** A representative example of an MHC-II-expressing (upper panel, scale bar = 8 μm) and a non-MHCII-expressing (lower panel, scale bar = 10 μm) engulfing CX3CR1⁺ cell is shown. Engulfing myeloid cells are marked with dashed circles and engulfed T cells with asterisks. Representative of n = 9 engulfing cells from two different experiments. **(H)** Columns reflect the counts of MHC-II⁺ and MHC-II⁻ cells among engulfing CX3CR1⁺ cells in EAE diseased mice (n = 9 engulfing cells from two different experiments). Statistical analyses for A and B were performed using one-way ANOVA with Tukey's post hoc test. Statistical analyses for D and E were performed using two-sided Student's t test. *, P < 0.05, **, P < 0.01.

first-defense-like process, as is known for their phagocytosis properties toward CNS-invading pathogens. In vivo, CNS-infiltrating myeloid cells may contribute to this T cell capture. However, microglia, which are present from the onset of the disease, are capable of forming the first line of defense against invading lymphocytes. Optimizing this first defense process may therefore represent a valuable therapeutic opportunity in neuroinflammatory diseases. Indeed, we were able to show that intrathecal therapeutic enhancement of GlcNAc exposure on

T cells was effective at ameliorating EAE disease symptoms. Similar beneficial effects were reported previously after oral GlcNAc administration in mild EAE (Grigorian et al., 2011), focusing so far only on peripheral effects and without providing mechanistic insights. Here, by applying GlcNAc intrathecally, we excluded peripheral effects and demonstrated that GlcNAc-mediated T cell reduction in the CNS causes disease amelioration. Our findings point toward T cell engulfment by CX3CR1⁺ myeloid cells as an early defense mechanism upon initial T cell

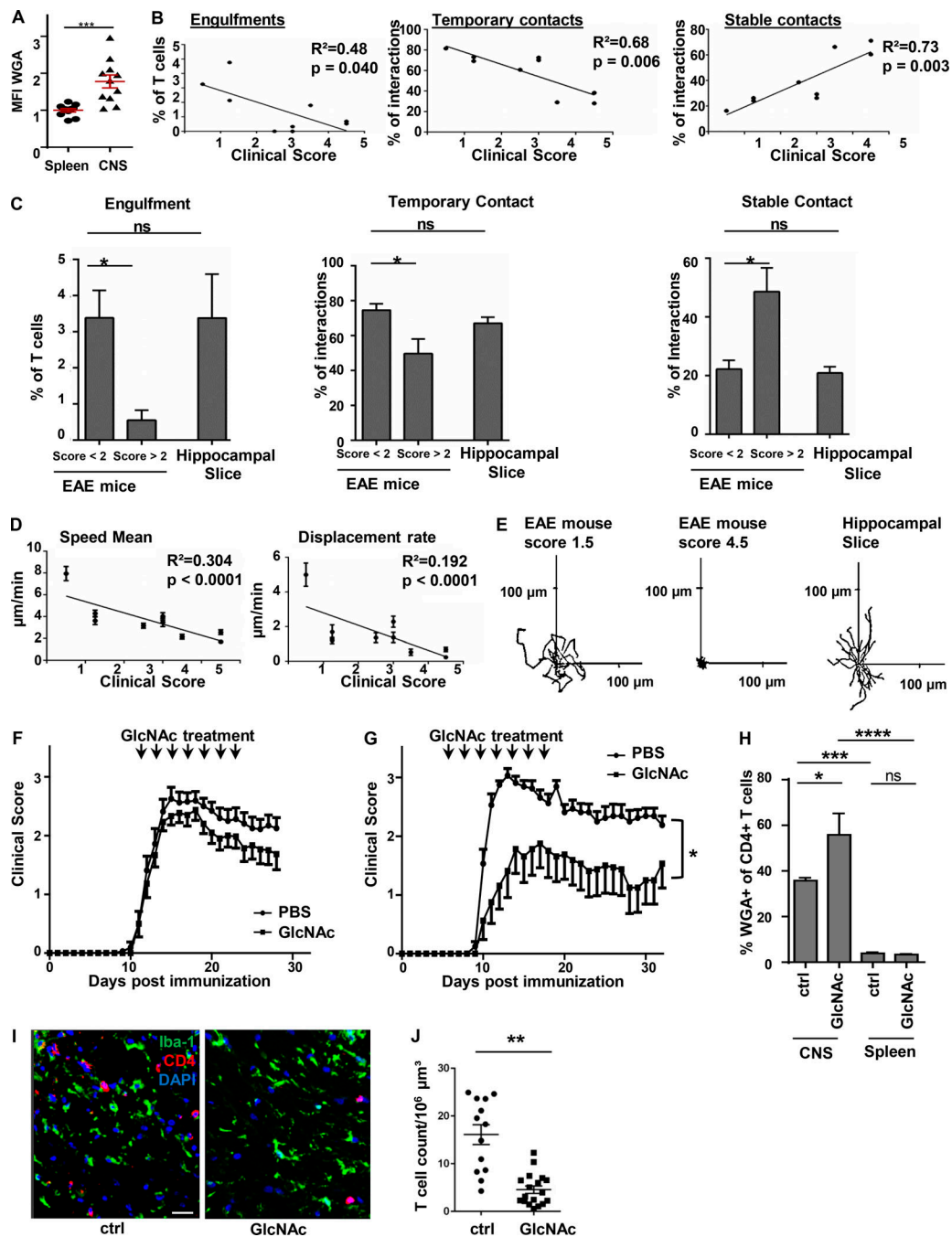


Figure 8. Enhanced GlcNAc exposure on T cell ameliorates EAE during the early disease course. (A) Flow cytometric analysis of WGA binding on living CD4⁺ T cells in the CNS and spleen of EAE diseased mice in actively immunized C57BL/6 mice normalized to splenic T cells ($n = 11$ mice from two different experiments). (B–E) EAE was induced in CX3CR1.GFPxRag^{-/-} and CX3CR1.GFPxRag^{+/-} mice (myeloid cells green) via the passive transfer of B6.2D2.RFP.Th17 cells (red). Interactions between myeloid cells and T cells as well as T cell motility parameters were imaged in vivo with intravital two-photon imaging and analyzed during different disease states. For hippocampal slice culture experiments, co-cultures of hippocampal slices from CX3CR1.GFP pups with pathogenic B6.2D2.CFP.Th17 cells were stained with Image-iT LIVE Red Caspase-3 and -7 Detection Kit to identify apoptotic cells, and only living T cells were included for further analysis. (B) Dots represent the percentages of engulfments, temporary contacts and stable contacts among the analyzed T cells in a randomly defined area of the CNS (brainstem) of EAE diseased mice in dependency on disease score. P values indicate whether the slope of linear regression is significantly nonzero ($n = 9$ mice from two different experiments). (C) Means (\pm SEM) of percentages of engulfments, temporary contacts, and stable contacts among the detected interactions or the detectable T cell count per region of interest were compared between mice exhibiting a score <2 ($n = 3$ mice from two different experiments), mice exhibiting a score >2 ($n = 6$ mice from two different experiments), and hippocampal slice cultures ($n = 12$ organotypic hippocampal slice cultures from eight different experiments). Statistical analysis was performed using one-sided Mann–Whitney U test. *, $P < 0.05$; ns, not significant. (D) Mean (\pm SEM) of T cell motility parameters in the CNS of EAE diseased mice in dependency on disease score. P values indicate whether the slope of linear regression is significantly nonzero ($n = 9$ mice, 30 T cells per mouse from two different experiments). (E) Normalization of all T cell tracks to a common starting point in a representative experiment of a hippocampal slice co-culture comparing a mouse exhibiting a clinical score of 1.5 and a mouse exhibiting a clinical score of 4.5. Each line represents one individual T cell. Representative of 9 mice from two different experiments. (F–J) EAE was induced actively in C57BL/6 mice and 5 μl

PBS or 5 μ l GlcNAc-solution (200 mM solved in PBS) were applied intrathecally every second day seven times, either starting at the onset of disease (day 11, F and H) or before the onset of the disease (day 7, G). **(F)** EAE course in PBS-treated vs. GlcNAc-treated mice ($n = 16$ PBS-treated mice, 15 GlcNAc-treated mice from 2 different experiments). **(G)** EAE course in PBS-treated vs. GlcNAc-treated mice. ($n = 8$ PBS-treated mice, 8 GlcNAc-treated mice from 2 different experiments). **(H)** Means (\pm SEM) of percentages of WGA binding T cells in the CNS and spleen of PBS (ctrl) and GlcNAc-treated mice. **(I and J)** Immunohistochemistry was performed to identify T cells in PBS-treated and GlcNAc-treated mice. **(I)** Shown are representative images of Iba-1 (green), CD4 (red), and DAPI (blue) in PBS-treated mice (ctrl, $n = 13$ slices of three different mice from two different experiments) and GlcNAc-treated mice (GlcNAc, $n = 18$ of three different mice from two different experiments), scale bar = 20 μ m, and **(J)** the quantification of CD4⁺ T cells. Statistical analysis in F, G, and J was performed using two-sided Student's *t* tests comparing the cumulative scores of the distinct groups. Statistical analysis in H was performed using one-way ANOVA with Tukey's post hoc test. *, $P < 0.05$; ***, $P < 0.001$; ****, $P < 0.0001$; ns, not significant.

invasion that is overcome later on in a full-blown inflammatory environment. The reasons for this shift are most likely functional changes due to microenvironment alterations in the course of the disease, since we were able to show that alternatively activated (versus classically activated) myeloid cells possess markedly increased engulfment. Importantly, although T cell removal from the CNS is beneficial during a T cell-mediated neuroinflammatory disease, this T cell removal could be harmful, such as in pathogen-mediated diseases, in which T cells are required to promote defense mechanisms in the CNS. Future studies are needed to analyze these engulfment processes in other disease contexts.

According to *in vitro* observations, cell-in-cell structures have, to date, been reported mostly for tumor cells (Yang and Li, 2012), and the use of different, mostly vaguely defined terms (e.g., entosis, [suicide] emperipolesis, phagoptosis, cytophagocytosis, or cannibalism) indicates that both the physiological significance and underlying pathways of these so-called cell-in-cell structures are still poorly understood (Brown and Neher, 2014; Overholtzer and Brugge, 2008). In our study, *in vivo* two-photon imaging as well as long-term follow up of slice cultures revealed full engulfment of viable T cells. Strikingly, some engulfed T cells were able to freely move through the glial cytoplasm, often even followed by escape from glial entrapment. In very few earlier neuropathologic reports based on occasional histological observations, cell-in-cell formation has been mentioned for lymphocytes in neurons (Hughes et al., 1968; Ng and Ling, 1999) and for oligodendrocytes in astrocytes (Shintaku and Yutani, 2004; Wu and Raine, 1992). The presently demonstrated engulfment and residence of T cells within myeloid cells may be reminiscent of entosis, a form of cell cannibalism (Krishna and Overholtzer, 2016). However, entotic cells, in contrast to Th17 cells, are reported to not expose the eat-me signal PS, which may explain why they can be rescued from cell death after engulfment. Furthermore, entosis has so far mostly been assigned to homotypic cell-in-cell interactions (i.e., among the same cell types) and in almost all reports is restricted to tumor cells (both in culture and *in vivo*). A potential role of entosis in a noncancerous context has not been reported so far.

In our study, inhibition of T cell activity or prevention of myeloid cell binding to GlcNAc on T cells resulted in inhibition of T cell engulfment by myeloid cells. GlcNAc has been discussed previously to promote the binding of apoptotic thymocytes to macrophages and their subsequent phagocytosis (Duvall et al., 1985). Of note, we were able to show that the engulfment of viable T cells was not driven by PS exposure, clearly identifying this process to be distinct from classic PS-mediated phagocytosis.

GlcNAc, which we showed here to be responsible for the engulfment of living T cells, is also expressed by bacteria, where it serves as a target molecule for pattern recognition receptors on phagocytes, resulting in the phagocytosis and removal of harmful CNS intruders (Nadesalingam et al., 2005; Zhang et al., 2015). Myeloid cell activation in organotypic slices led to an up-regulation of the lectin CD206, which is a receptor for GlcNAc (Taylor et al., 1992, 2005), and was accompanied by increased engulfment processes, thus indicating that an increase of myeloid cell activity supports increased abilities to capture living T cells. Interestingly, CNS-invading CD4⁺ T cells during EAE showed higher GlcNAc expression than their peripheral counterparts, thus emphasizing the importance of the GlcNAc-lectin pathway within the CNS.

Enhancement of GlcNAc-dependent engulfment of living cells was sufficient to significantly decrease EAE severity, emphasizing the biological relevance of T cell engulfment by myeloid cells. Although the percentage of engulfments among myeloid cell-T cell interactions was in the single digits, it should be pointed out that these percentages represent only a short temporal snapshot of the engulfment processes, especially compared with the large number of temporal screening contacts taking place in the CNS, thus likely underestimating the total cell count of removed cells.

Altogether, we identified highly dynamic interaction modes between myeloid cells and T cells within the brain, reflecting the attempt of myeloid cells to remove viable potentially pathogenic T cells from the CNS in a GlcNAc-mediated pathway, in order to preserve tissue homeostasis during early inflammation. The unique ability of some T cells to migrate through myeloid cells without subsequent cell death and instead escape from engulfment reveals a newly discovered mechanism highlighting their pathological potency in CNS inflammation and limitation of defense capacity in neuroinflammation. Overall, the findings reported here explore a novel, primarily protective role of myeloid cells in early neuroinflammation and may open new avenues for impacting neurological disorders such as MS.

Materials and methods

Mice

All mice were kept under specific pathogen-free conditions. B6.CX3CR1^{+/GFP} and B6.CX3CR1^{+/GFP}orGFP/GFP.Rag^{-/-or+/-} mice were used for *in vivo* imaging as indicated. B6.CX3CR1^{GFP/GFP} mice were used for *ex vivo* imaging of myeloid cells, as genotyping of pups from heterozygous breeding is not feasible before slice preparation (Jung et al., 2000). We confirmed similar

interactions in heterozygous organotypic slices, gained by crossing B6.CX3CR1^{GFP/GFP} mice with C57BL/6 mice (Fig. S2). Throughout the article, CX3CR1^{GFP} is used for simplicity and better readability. B6.2D2.RFP mice and B6.2D2.CFP mice, in which all CD4⁺ T cells are MOG₃₅₋₅₅ specific, were obtained by crossbreeding B6.acRFP and B6.CFP with B6.2D2 mice (Bettelli et al., 2003; Hadjantonakis et al., 2002; Luche et al., 2007). These mice were used for T cell cultures. All animal experiments were approved by local authorities (Landesuntersuchungsamt Rheinlandpfalz) and performed in accordance with German Animal Protection Laws.

EAE

For passive-transfer EAE, 10–40 × 10⁶ B6.2D2.RFP cells were injected intravenously into recipient mice (B6.CX3CR1^{+/GFP}, B6.CX3CR1^{+/GFP} or GFP/GFP, Rag^{-/-} or +/+) and pertussis toxin (400 ng/mouse) was injected on the day of transfer and day 2 following transfer. If Rag^{-/-} mice were used, no pertussis toxin was injected. For active EAE, C57BL/6 mice were immunized subcutaneously with 200 µg myelin oligodendrocyte protein MOG₃₅₋₅₅ in 200 µl CFA emulsion. Additionally, C57BL/6 mice received 200 ng pertussis toxin (Hooke kit; Hooke Laboratories) intraperitoneally at the time of immunization and 24 h later. For intrathecal treatment with GlcNAc (5 µl of 200 mM GlcNAc dissolved in PBS) and PBS (5 µl), mice were shortly anesthetized using isoflurane. The lumbar region was shaved and disinfected. Application was performed into the spinal canal between L5 and L6 every second day seven times. Mice were scored for clinical symptoms daily, and signs of EAE were translated into clinical score as follows: 0, no detectable signs of EAE; 0.5, tail weakness; 1, complete tail paralysis; 2, partial hindlimb paralysis or ataxia; 2.5, unilateral complete hindlimb paralysis; 3, complete bilateral hindlimb paralysis or severe ataxia; 3.5, complete hindlimb paralysis and partial forelimb paralysis; 4, total paralysis of forelimbs and hindlimbs (mice with a score >3.5 to be killed); and 5, death.

T cell culture

Procedures were similar to those reported previously (Siffrin et al., 2009, 2010). In brief, cells from B6.2D2.CFP or B6.2D2.RFP mice were isolated from spleen and lymph nodes (axial and cranial), and magnetic bead-based cell sorts (Miltenyi) were performed. Naive CD4⁺CD62L^{hi} cells were stimulated with 2 µg/ml αCD3 (1452-C11; BD Biosciences) in the presence of irradiated CD90⁺-depleted C57BL/6 splenocytes, and culture medium was enriched with the following cytokines: for Th17 differentiation, 3 ng/ml TGF-β, 20 ng/ml IL-23, and 20 ng/ml IL-6 (all R&D Systems); for Th2 differentiation, 10 ng/ml IL-4 (R&D Systems), 10 µg/ml αIFNγ (XMG1.2; BioXcell), and 10 µg/ml αIL-12 (C17.8; BioXcell); for T reg cell differentiation, 3 ng/ml TGF-β (R&D Systems), 10 µg/ml αIL-12 (C17.8; BioXcell), and 10 µg/ml αIFNγ (XMG1.2; BioXcell). After 3 d of culture, cells were split, and T cell culture medium was enriched with 50 U/ml IL-2 and 10 ng/ml IL-23 for Th17 or 100 U/ml IL-2 and 10 ng/ml IL-4 (all R&D Systems) for Th2 cells. T reg cells were split, and fresh IL-2 (100 U/ml) was added after 2 and 4 d of culture. Th17 cells were either used for co-cultures with hippocampal slices after 5 d of

culture or restimulated after 1 week with 2 µg/ml anti-CD3 in the presence of irradiated CD90⁺-depleted C57BL/6 splenocytes and treated with 0.75 ng/ml TGF-β, 20 ng/ml IL-23, and 10 ng/ml IL-6. If restimulated, cells were used 3 d after restimulation for further experiments (co-culture with organotypic hippocampal slices or induction of passive-transfer EAE).

For GlcNAc enhancement experiments, naive CD4⁺CD62L^{hi} T cells were treated on day 0 of culture with 20 mM GlcNAc. For Th17 differentiation, 3 ng/ml TGF-β, 20 ng/ml IL-23, and 20 ng/ml IL-6 (all R&D Systems) were additionally added. On day 3, T cells were harvested and transferred on an anti-CD3/anti-CD28-precoated 48-well plate, and 20 mM GlcNAc was added to the GlcNAc-pretreated group. WGA binding was assessed on day 5.

Organotypic hippocampal slice culture

For organotypic hippocampal slice cultures, postnatal day 3–6 B6.CX3CR1^{GFP/GFP} pups were decapitated, and brains were rapidly removed and transferred to ice-cold preparation medium (MEM) containing 2 mM glutamine, adjusted to pH 7.35. Both hemispheres were separated and the meninges removed, and hippocampi were isolated with entorhinal cortex attached and coronally cut (300 µm) using a McILWAIN tissue chopper. Intact hippocampal slices were transferred onto Millicell cell culture inserts (Merck Millipore) positioned in each well of a 6-well plate (Greiner) containing 1.2 ml culture medium (48% MEM, 24% basal medium Eagle, 24% heat-inactivated horse serum, 2 mM glutamine, and 0.6% glucose, pH 7.2) and incubated at 37°C, 95%/5% O₂/CO₂. The medium was changed 24 h after plating and then every other day. After 7–14 d in vitro, hippocampal slices were used for experiments.

For co-cultures, either 10⁵ Th17 cells or 10⁵ Th2 cells were added in a volume of 10 µl directly on top of the hippocampal slices and incubated at 37°C, 95%/5% O₂/CO₂ for 24 h or, in the case of GlcNAc enhancement experiments, 4 h. At the time the T cells were added, slices were also optionally treated with Annexin V (10 µg/ml), Wortmannin (2.5–5 µM), or MOG₃₅₋₅₅ peptide (100 µg/ml; Genscript) as indicated. For LPS (classic activation) and LPS/dexamethasone/IL-4 preactivation (alternative activation), organotypic slices were treated with LPS (1 µg/ml) or LPS (1 µg/ml), dexamethasone (5 × 10⁻⁷ M), and IL-4 (10 ng/ml) for 24 h before T cell addition. LPS, dexamethasone, and IL-4 were kept in the medium during the co-culture. To distinguish viable and apoptotic T cells, co-cultures were stained with the Image-iT LIVE Red Caspase-3 and -7 Detection Kit (Thermo Fisher Scientific) 30 to 60 min before imaging. Competitive GlcNAc (20 mM) treatment was performed 24 h and additionally 20 min before T cell addition. GlcNAc was kept in the medium during the co-culture. For GlcNAc enhancement experiments, GlcNAc-pretreated T cells (see T cell culture) were added. RGDS (Arg-Gly-Asp-Ser) treatment (1 mM) was performed 24 h and additionally 20 min before T cell addition. RGDS was kept in the medium during the co-culture.

Intravital two-photon imaging

Operation procedures and two-photon laser scanning microscopy were performed as described previously (Herz et al., 2010; Luchtman et al., 2016; Siffrin et al., 2009, 2010). Mice were

anesthetized using 1.5% isoflurane in oxygen/nitrous oxide (1:2) and then continuously respirated with a facemask. Mice were transferred to a custom-built operation and microscopy table and fixed in a hanging position. The brainstem was exposed by the removal of the musculature above the dorsal neck area and removal of the dura mater using a microscope. The head was inclined for access to deeper brainstem regions. A sterile agarose patch (0.5% in 0.9% NaCl solution) was installed on the exposed brain surface. During surgery and microscopy, body temperature was maintained at 37°C. Anesthesia depth was controlled by continuous CO₂ measurements of exhaled gas and recorded with a CI-240 Microcapnograph (Columbus Instruments). Imaging was performed in the brainstem. We applied dual near-infrared and infrared excitation of the live brainstem at 850 nm by an automatically tunable Ti/Sa laser (Mai Tai HP; Spectra Physics) and 1110 nm by an optical parametric oscillator (APE) pumped by the Ti/Sa laser. Using a TriMScope I multiphoton system from LaVision Biotec, volumes of 300 μm × 300 μm × 72 μm were acquired over time and exported as TIFFs for 3D analyses.

For the ex vivo slice experiments, slices were transferred onto the stage of a Leica TCS-MP5 multi-photon system with heated, humidified, and gassed (95% O₂/5% CO₂) chamber within a Ludin enclosure and volumes of 300 μm × 300 μm at variable depth (max 80 μm) acquired with a Leica HCX IRAPO L 25×/0.95 W objective at 1000 nm to visualize the CX3CR1^{GFP} myeloid cells and B6.2d2.RFP.Th17 cells. For imaging CX3CR1^{GFP} myeloid cells and B6.2d2.CFP.Th17 cells that were alive (CFP) or stained with Image-iT LIVE Red Caspase-3 and -7, as well as imaging long term (beyond 20 min), we used the TriMScope I from LaVision Biotec with the Bold-Line series of stage top incubators from Okolab (Pozzuoli, NA).

Analysis of two-photon imaging results

TIFF and LIF files were imported into 3D reconstruction software Imaris (Bitplane, version 8.1.2). T cell tracks were created using the tracking tool implemented in Imaris software and manually corrected. Contact types and durations were determined manually with 3D rotation and surface analysis to verify contacts. Temporary contacts were defined as contacts lasting <10 min and stable contacts as contacts lasting ≥10 min. Engulfment-related processes (EPs) were subdivided into engulfment (T cell is fully surrounded by the myeloid cell), escape (T cell moves through the myeloid cell and escapes), and clear attempt to engulf (myeloid cell actively prolongs processes to engulf T cells). On average, 20–100 T cells were analyzed per region of interest (maximum 300 μm × 300 μm × 80 μm) in one organotypic hippocampal slice. For T cell motility analysis, a maximum of 30 cells reflecting the mean velocities per video were included into further analyses. Noise reduction was achieved by the software's "medium filter."

Histological staining

Immunohistochemistry was performed with co-cultures of organotypic hippocampal slices from CX3CR1^{GFP} mice with 2D2 T cells and spinal cord sections of EAE diseased CX3CR1^{GFP} animals. Iba-1⁺/CX3CR1⁺ myeloid cells were stained with anti-mouse GFP (polyclonal-rabbit; Abcam; 270F3 mouse; Synaptic Systems) or anti-mouse Iba-1 (polyclonal-rabbit; Abcam) and

anti-rabbit-AF488 (polyclonal; Thermo Fisher Scientific). CD4 was stained with anti-mouse CD4-AF647 (RM4-5 rat; BD Biosciences). MHC-II was stained with anti-mouse MHC-II (2G9 rat; BD Biosciences), CD206 with anti-mouse CD206 (C068C2 rat; BioLegend) and anti-rat-AF568 (polyclonal, Thermo Fisher Scientific), CD31 with anti-mouse CD31 (polyclonal-rabbit, Thermo Fisher Scientific) and anti-rabbit-AF647 (polyclonal; Thermo Fisher Scientific). The cell nucleus was stained with DAPI (Thermo Fisher Scientific).

Flow cytometry analysis

For flow cytometric analysis of T cells in vitro, Th17 cells were harvested and stained with fluorescently labeled αCD4 (RM4-5), αCD44 (IM7), αCD25 (PC61; BD Biosciences or BioLegend), and WGA (Thermo Fisher Scientific). Dead cells were identified using either propidium iodide or fixable viable stain-V450 (BD Biosciences). For intracellular staining, cells were fixated with 2% paraformaldehyde after 4 h of stimulation in the presence of Brefeldin A. IL-17 expression was determined using fluorescently labeled αIL-17 (eBio17B7; BD Biosciences). PS exposure was determined via Annexin V staining kit from eBioscience. For flow cytometric analysis of T cells and myeloid cells ex vivo, CNS and spleen tissue was prepared as described previously (Wasser et al., 2016). Cells were stained with fluorescently labeled αCD4 (RM4-5; BD Biosciences), WGA (Thermo Fisher Scientific), αCD11b (M1/70; Thermo Fisher Scientific), αCD45 (30-F11; Thermo Fisher Scientific), αLy6C/G (RB6-8C5; BD Biosciences), αCD206 (C068C2; BioLegend), and IgG2ακ-BV421 (RTK2758; BioLegend) as indicated. For flow cytometric analysis of myeloid cells in organotypic hippocampal slices (≥7 d in culture), organotypic slices from CX3CR1^{GFP} pups were digested with 10 mg/ml Collagenase/Dispase (Sigma), 10 mg/ml Collagenase (Sigma), and 200 U/ml DNase (Roche). After incubation for 30 min at 37°C, the tissue was removed from the cell culture inserts and put through a mesh (100 μm), and mononuclear cells were separated by 30/70 Percoll; i.e., 70% Percoll (Sigma) in PBS (Sigma) was overlaid with cells resuspended in 30% Percoll in IMDM solution (Gibco) and then centrifuged at 750 *g* for 20 min. Mononuclear cells were collected at the interface and stained as indicated with fluorescently labeled αCD45 (30-F11; Thermo Fisher Scientific), αCD11b (M1/70, Thermo Fisher Scientific), αCD206 (C068C2; BioLegend), and IgG2ακ-BV421 (RTK2758; BioLegend). All gating strategies are provided in Fig. S3.

Statistical analysis

All data were analyzed using GraphPad Prism 6 (GraphPad Software). Mean group differences were investigated by one-way ANOVA followed by Tukey's multiple comparison test, Mann-Whitney *U* test, or independent-sample two-tailed *t* tests. The significance level was set at 0.05. Pie charts reflect the mean of the relative interaction distributions per analyzed video. If normalization was performed, each parameter was normalized to the mean of the control group from the respective slice preparation.

Online supplemental material

Fig. S1 shows the effect on GlcNAc exposure on the engulfment of apoptotic cells and the distribution of CD206 expression in

organotypic hippocampal slices and the CNS of EAE diseased mice. **Fig. S2** shows the interactions of T cells and myeloid cells in organotypic hippocampal slices. **Fig. S3** shows all gating strategies for flow cytometric analysis shown in the main text. **Video 1** shows surface-reconstructed intravital two-photon live imaging of an escaping T cell in vivo. **Video 2** shows two-photon live imaging of Th17 cell–myeloid cell interactions ex vivo. **Video 3** shows two-photon live imaging of a temporary contact ex vivo. **Video 4** shows two-photon live imaging of a stable contact ex vivo. **Video 5** shows two-photon live imaging of a stable engulfment ex vivo. **Video 6** shows two-photon live imaging of an escape following walkthrough ex vivo. **Video 7** shows two-photon live imaging of an engulfment attempt. **Video 8** shows two-photon live imaging of a long-term engulfment. **Video 9** shows two-photon live imaging of a long-term escape. **Video 10** shows in vivo dynamics of T cell–myeloid cell interactions during early and chronic disease.

Acknowledgments

The authors thank Christin Liefänder, Heike Ehrengard, Ilse Graevenitz, Christine Oswald, and Jerome Birkenstock for excellent technical assistance and Cheryl Ernest and Rosalind Gilchrist for proofreading and editing the manuscript.

This study was supported by the Deutsche Forschungsgemeinschaft (grant SFB CRC-TR-128 to F. Zipp and S. Bittner, grants SFB 1080 and SFB CRC-1292 to F. Zipp, and grant TP BI1822/1-1 to S. Bittner) and the Hertie Foundation (mylab to S. Bittner).

Author contributions: B. Wasser, D. Luchtman, S. Bittner, and F. Zipp conceived the study. B. Wasser and D. Luchtman designed and performed the main experimental work and analyzed the data. D. Luchtman, K. Robohm, B. Wasser, and J. Löffel performed the isolation of hippocampal slices. K. Birkner performed EAE experiments. B. Wasser, K. Birkner, C.F. Vogelaar, and A. Stroh performed data analysis. B. Wasser, D. Luchtman, F. Zipp, and S. Bittner evaluated all data and wrote and edited the manuscript.

Disclosures: The authors declare no competing interests exist.

Submitted: 6 May 2019

Revised: 20 September 2019

Accepted: 17 January 2020

References

- Ajami, B., N. Samusik, P. Wieghofer, P.P. Ho, A. Crotti, Z. Bjornson, M. Prinz, W.J. Fantl, G.P. Nolan, and L. Steinman. 2018. Single-cell mass cytometry reveals distinct populations of brain myeloid cells in mouse neuroinflammation and neurodegeneration models. *Nat. Neurosci.* 21: 541–551. <https://doi.org/10.1038/s41593-018-0100-x>
- Aktas, O., A. Smorodchenko, S. Brocke, C. Infante-Duarte, U. Schulze Topphoff, J. Vogt, T. Prozorovski, S. Meier, V. Osmanova, E. Pohl, et al. 2005. Neuronal damage in autoimmune neuroinflammation mediated by the death ligand TRAIL. *Neuron*. 46:421–432. <https://doi.org/10.1016/j.neuron.2005.03.018>
- Bettelli, E., M. Pagany, H.L. Weiner, C. Lington, R.A. Sobel, and V.K. Kuchroo. 2003. Myelin oligodendrocyte glycoprotein-specific T cell receptor transgenic mice develop spontaneous autoimmune optic neuritis. *J. Exp. Med.* 197:1073–1081. <https://doi.org/10.1084/jem.20021603>
- Brown, G.C., and J.J. Neher. 2014. Microglial phagocytosis of live neurons. *Nat. Rev. Neurosci.* 15:209–216. <https://doi.org/10.1038/nrn3710>
- Cahalan, M.D., and I. Parker. 2008. Choreography of cell motility and interaction dynamics imaged by two-photon microscopy in lymphoid organs. *Annu. Rev. Immunol.* 26:585–626. <https://doi.org/10.1146/annurev.immunol.24.021605.090620>
- Dendrou, C.A., L. Fugger, and M.A. Friese. 2015. Immunopathology of multiple sclerosis. *Nat. Rev. Immunol.* 15:545–558. <https://doi.org/10.1038/nri3871>
- Duvall, E., A.H. Wyllie, and R.G. Morris. 1985. Macrophage recognition of cells undergoing programmed cell death (apoptosis). *Immunology*. 56: 351–358.
- Falcão, A.M., D. van Bruggen, S. Marques, M. Meijer, S. Jäkel, E. Agirre, E.M. Samudryata, E.M. Floriddia, D.P. Vanichkina, C. Ffrench-Constant, et al. 2018. Disease-specific oligodendrocyte lineage cells arise in multiple sclerosis. *Nat. Med.* 24:1837–1844. <https://doi.org/10.1038/s41591-018-0236-y>
- Franco, R., and D. Fernández-Suárez. 2015. Alternatively activated microglia and macrophages in the central nervous system. *Prog. Neurobiol.* 131: 65–86. <https://doi.org/10.1016/j.pneurobio.2015.05.003>
- Geissmann, F., S. Jung, and D.R. Littman. 2003. Blood monocytes consist of two principal subsets with distinct migratory properties. *Immunity*. 19: 71–82. [https://doi.org/10.1016/S1074-7613\(03\)00174-2](https://doi.org/10.1016/S1074-7613(03)00174-2)
- Giles, D.A., J.M. Washnock-Schmid, P.C. Duncker, S. Dahlawi, G. Ponath, D. Pitt, and B.M. Segal. 2018. Myeloid cell plasticity in the evolution of central nervous system autoimmunity. *Ann. Neurol.* 83:131–141. <https://doi.org/10.1002/ana.25128>
- Goldmann, T., P. Wieghofer, P.F. Müller, Y. Wolf, D. Varol, S. Yona, S.M. Brendecke, K. Kierdorf, O. Staszewski, M. Datta, et al. 2013. A new type of microglia gene targeting shows TAK1 to be pivotal in CNS autoimmune inflammation. *Nat. Neurosci.* 16:1618–1626. <https://doi.org/10.1038/nn.3531>
- Goverman, J. 2009. Autoimmune T cell responses in the central nervous system. *Nat. Rev. Immunol.* 9:393–407. <https://doi.org/10.1038/nri2550>
- Grigorian, A., L. Araujo, N.N. Naidu, D.J. Place, B. Choudhury, and M. Demetriou. 2011. N-acetylglucosamine inhibits T-helper 1 (Th1)/T-helper 17 (Th17) cell responses and treats experimental autoimmune encephalomyelitis. *J. Biol. Chem.* 286:40133–40141. <https://doi.org/10.1074/jbc.M111.277814>
- Hadjantonakis, A.K., S. Macmaster, and A. Nagy. 2002. Embryonic stem cells and mice expressing different GFP variants for multiple non-invasive reporter usage within a single animal. *BMC Biotechnol.* 2:11. <https://doi.org/10.1186/1472-6750-2-11>
- Heneka, M.T., M.P. Kummer, and E. Latz. 2014. Innate immune activation in neurodegenerative disease. *Nat. Rev. Immunol.* 14:463–477. <https://doi.org/10.1038/nri3705>
- Heppner, F.L., M. Greter, D. Marino, J. Falsig, G. Raivich, N. Hövelmeyer, A. Waisman, T. Rüllicke, M. Prinz, J. Priller, et al. 2005. Experimental autoimmune encephalomyelitis repressed by microglial paralysis. *Nat. Med.* 11:146–152. <https://doi.org/10.1038/nm1177>
- Herz, J., V. Siffrin, A.E. Hauser, A.U. Brandt, T. Leuenberger, H. Radbruch, F. Zipp, and R.A. Niesner. 2010. Expanding two-photon intravital microscopy to the infrared by means of optical parametric oscillator. *Biophys. J.* 98:715–723. <https://doi.org/10.1016/j.bpj.2009.10.035>
- Hughes, D., C.S. Raine, and E.J. Field. 1968. Invasion of neurones in vitro by non immune lymphocytes. An electron microscopic study. *Br. J. Exp. Pathol.* 49:356–359.
- Jiang, Z., J.X. Jiang, and G.-X. Zhang. 2014. Macrophages: a double-edged sword in experimental autoimmune encephalomyelitis. *Immunol. Lett.* 160:17–22. <https://doi.org/10.1016/j.imlet.2014.03.006>
- Jolivel, V., F. Bicker, F. Binamé, R. Ploen, S. Keller, R. Gollan, B. Jurek, J. Birkenstock, L. Poisa-Beiro, J. Bruttger, et al. 2015. Perivascular microglia promote blood vessel disintegration in the ischemic penumbra. *Acta Neuropathol.* 129:279–295. <https://doi.org/10.1007/s00401-014-1372-1>
- Jung, S., J. Aliberti, P. Graemmel, M.J. Sunshine, G.W. Kreutzberg, A. Sher, and D.R. Littman. 2000. Analysis of fractalkine receptor CX(3)CR1 function by targeted deletion and green fluorescent protein reporter gene insertion. *Mol. Cell. Biol.* 20:4106–4114. <https://doi.org/10.1128/MCB.20.11.4106-4114.2000>
- Kerschensteiner, M., C. Stadelmann, G. Dechant, H. Wekerle, and R. Hohlfeld. 2003. Neurotrophic cross-talk between the nervous and immune systems: implications for neurological diseases. *Ann. Neurol.* 53:292–304. <https://doi.org/10.1002/ana.10446>
- Krishna, S., and M. Overholtzer. 2016. Mechanisms and consequences of entosis. *Cell. Life Sci.* 73:2379–2386. <https://doi.org/10.1007/s00018-016-2207-0>

- Lampron, A., A. Laroche, N. Laflamme, P. Préfontaine, M.-M. Plante, M.G. Sánchez, V.W. Yong, P.K. Stys, M.-È. Tremblay, and S. Rivest. 2015. Inefficient clearance of myelin debris by microglia impairs remyelinating processes. *J. Exp. Med.* 212:481–495. <https://doi.org/10.1084/jem.20141656>
- Lobo-Silva, D., G.M. Carriche, A.G. Castro, S. Roque, and M. Saraiva. 2017. Interferon- β regulates the production of IL-10 by toll-like receptor-activated microglia. *Glia*. 65:1439–1451. <https://doi.org/10.1002/glia.23172>
- Lu, Z., M.R. Elliott, Y. Chen, J.T. Walsh, A.L. Klibanov, K.S. Ravichandran, and J. Kipnis. 2011. Phagocytic activity of neuronal progenitors regulates adult neurogenesis. *Nat. Cell Biol.* 13:1076–1083. <https://doi.org/10.1038/ncb2299>
- Luche, H., O. Weber, T. Nageswara Rao, C. Blum, and H.J. Fehling. 2007. Faithful activation of an extra-bright red fluorescent protein in “knock-in” Cre-reporter mice ideally suited for lineage tracing studies. *Eur. J. Immunol.* 37:43–53. <https://doi.org/10.1002/eji.200636745>
- Luchtman, D., R. Gollan, E. Ellwardt, J. Birkenstock, K. Robohm, V. Siffrin, and F. Zipp. 2016. In vivo and in vitro effects of multiple sclerosis immunomodulatory therapeutics on glutamatergic excitotoxicity. *J. Neurochem.* 136:971–980. <https://doi.org/10.1111/jnc.13456>
- Nadesalingam, J., A.W. Dodds, K.B. Reid, and N. Palaniyar. 2005. Mannose-binding lectin recognizes peptidoglycan via the N-acetyl glucosamine moiety, and inhibits ligand-induced proinflammatory effect and promotes chemokine production by macrophages. *J. Immunol.* 175:1785–1794. <https://doi.org/10.4049/jimmunol.175.3.1785>
- Napoli, I., and H. Neumann. 2010. Protective effects of microglia in multiple sclerosis. *Exp. Neurol.* 225:24–28. <https://doi.org/10.1016/j.expneurol.2009.04.024>
- Ng, Y.K., and E.A. Ling. 1999. Emperipolesis of lymphoid cells in vagal efferent neurons following an intraneural injection of ricin into the vagus nerve in rats. *Neurosci. Lett.* 270:153–156. [https://doi.org/10.1016/S0304-3940\(99\)00490-5](https://doi.org/10.1016/S0304-3940(99)00490-5)
- Nimmerjahn, A., F. Kirchhoff, and F. Helmchen. 2005. Resting microglial cells are highly dynamic surveillants of brain parenchyma in vivo. *Science*. 308:1314–1318. <https://doi.org/10.1126/science.1110647>
- Notter, M.F., and J.F. Leary. 1987. Surface glycoproteins of differentiating neuroblastoma cells analyzed by lectin binding and flow cytometry. *Cytometry*. 8:518–525. <https://doi.org/10.1002/cyto.990080513>
- Olah, M., S. Amor, N. Brouwer, J. Vinet, B. Eggen, K. Biber, and H.W. Boddeke. 2012. Identification of a microglia phenotype supportive of remyelination. *Glia*. 60:306–321. <https://doi.org/10.1002/glia.21266>
- Overholtzer, M., and J.S. Brugge. 2008. The cell biology of cell-in-cell structures. *Nat. Rev. Mol. Cell Biol.* 9:796–809. <https://doi.org/10.1038/nrm2504>
- Paterka, M., V. Siffrin, J.O. Voss, J. Werr, N. Hoppmann, R. Gollan, P. Belikan, J. Bruttger, J. Birkenstock, S. Jung, et al. 2016. Gatekeeper role of brain antigen-presenting CD11c+ cells in neuroinflammation. *EMBO J.* 35: 89–101. <https://doi.org/10.15252/embj.201591488>
- Ponomarev, E.D., K. Maresz, Y. Tan, and B.N. Dittel. 2007. CNS-derived interleukin-4 is essential for the regulation of autoimmune inflammation and induces a state of alternative activation in microglial cells. *J. Neurosci.* 27:10714–10721. <https://doi.org/10.1523/JNEUROSCI.1922-07.2007>
- Savill, J. 1997. Recognition and phagocytosis of cells undergoing apoptosis. *Br. Med. Bull.* 53:491–508. <https://doi.org/10.1093/oxfordjournals.bmb.a011626>
- Schafer, D.P., and B. Stevens. 2015. Microglia Function in Central Nervous System Development and Plasticity. *Cold Spring Harb. Perspect. Biol.* 7: a020545. <https://doi.org/10.1101/cshperspect.a020545>
- Shemer, A., D. Erny, S. Jung, and M. Prinz. 2015. Microglia Plasticity During Health and Disease: An Immunological Perspective. *Trends Immunol.* 36: 614–624. <https://doi.org/10.1016/j.it.2015.08.003>
- Shintaku, M., and C. Yutani. 2004. Oligodendrocytes within astrocytes (“emperipolesis”) in the white matter in Creutzfeldt-Jakob disease. *Acta Neuropathol.* 108:201–206. <https://doi.org/10.1007/s00401-004-0880-9>
- Sierra, A., O. Abiega, A. Shahraz, and H. Neumann. 2013. Janus-faced microglia: beneficial and detrimental consequences of microglial phagocytosis. *Front. Cell. Neurosci.* 7:6. <https://doi.org/10.3389/fncel.2013.00006>
- Siffrin, V., A.U. Brandt, H. Radbruch, J. Herz, N. Boldakowa, T. Leuenberger, J. Werr, A. Hahner, U. Schulze-Topphoff, R. Nitsch, and F. Zipp. 2009. Differential immune cell dynamics in the CNS cause CD4+ T cell compartmentalization. *Brain*. 132:1247–1258. <https://doi.org/10.1093/brain/awn354>
- Siffrin, V., H. Radbruch, R. Glumm, R. Niesner, M. Paterka, J. Herz, T. Leuenberger, S.M. Lehmann, S. Luenstedt, J.L. Rinnenthal, et al. 2010. In vivo imaging of partially reversible th17 cell-induced neuronal dysfunction in the course of encephalomyelitis. *Immunity*. 33:424–436. <https://doi.org/10.1016/j.immuni.2010.08.018>
- Siffrin, V., J. Birkenstock, D.W. Luchtman, R. Gollan, J. Baumgart, R.A. Niesner, O. Griesbeck, and F. Zipp. 2015. FRET based ratiometric Ca²⁺ imaging to investigate immune-mediated neuronal and axonal damage processes in experimental autoimmune encephalomyelitis. *J. Neurosci. Methods*. 249:8–15. <https://doi.org/10.1016/j.jneumeth.2015.04.005>
- Taylor, M.E., K. Bezouska, and K. Drickamer. 1992. Contribution to ligand binding by multiple carbohydrate-recognition domains in the macrophage mannose receptor. *J. Biol. Chem.* 267:1719–1726.
- Taylor, P.R., S. Gordon, and L. Martinez-Pomares. 2005. The mannose receptor: linking homeostasis and immunity through sugar recognition. *Trends Immunol.* 26:104–110. <https://doi.org/10.1016/j.it.2004.12.001>
- Wasser, B., G. Pramanik, M. Hess, M. Klein, F. Luessi, K. Dornmair, T. Bopp, F. Zipp, and E. Witsch. 2016. Increase of Alternatively Activated Antigen Presenting Cells in Active Experimental Autoimmune Encephalomyelitis. *J. Neuroimmune Pharmacol.* 11:721–732. <https://doi.org/10.1007/s11481-016-9696-3>
- Wu, E., and C.S. Raine. 1992. Multiple sclerosis. Interactions between oligodendrocytes and hypertrophic astrocytes and their occurrence in other, nondemyelinating conditions. *Lab. Invest.* 67:88–99.
- Yang, Y.-Q., and J.-C. Li. 2012. Progress of research in cell-in-cell phenomena. *Anat. Rec. (Hoboken)*. 295:372–377. <https://doi.org/10.1002/ar.21537>
- Zhang, X.-H., Y.-H. Shi, and J. Chen. 2015. Molecular characterization of a transmembrane C-type lectin receptor gene from ayu (*Plecoglossus altivelis*) and its effect on the recognition of different bacteria by monocytes/macrophages. *Mol. Immunol.* 66:439–450. <https://doi.org/10.1016/j.molimm.2015.05.009>

Supplemental material

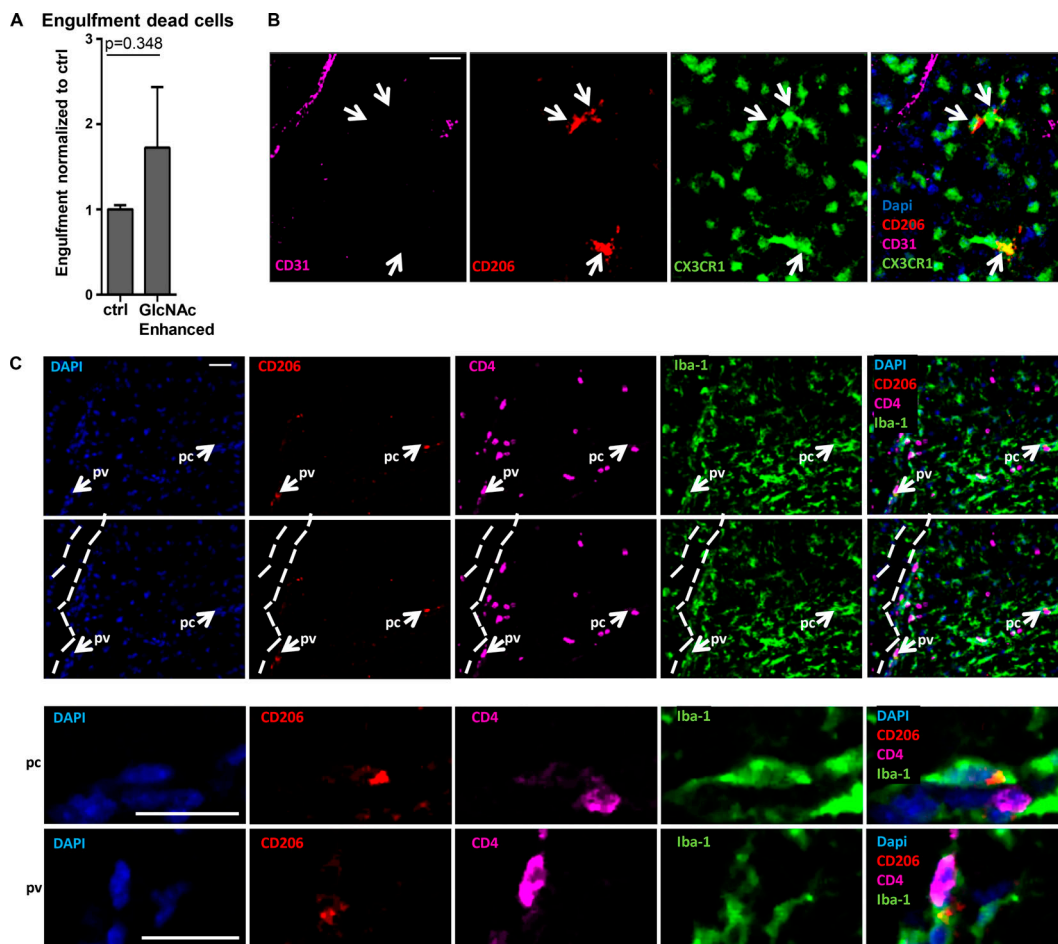


Figure S1. **Relevance of GlcNAc and CD206 during engulfment.** (A) Control Th17-skewed cells and GlcNAc-pretreated Th17-skewed cells were co-cultured with organotypic hippocampal slices. Co-cultures of organotypic hippocampal slices from CX3CR1^{GFP} pups with pathogenic B6.2D2.CFP.Th17 cells were stained with Image-iT LIVE Red Caspase-3 and -7 Detection Kit to identify apoptotic cells and imaged over a time period of 20 min. Only apoptotic T cells were considered for further analyses. Mean (\pm SEM) percentages of engulfment rate among the interactions of GlcNAc-pretreated Th17-skewed cells in organotypic hippocampal slices ($n = 4$ organotypic slices from three different experiments) normalized to the GlcNAc-untreated control group ($n = 4$ organotypic slices from three different experiments). Statistical analysis was performed using two-sided Student's *t* tests. (B) Representative visualization of CD31 (magenta), CD206 (red), CX3CR1 (green), and DAPI (blue), in dexamethasone/LPS/IL-4-treated organotypic hippocampal slice cultures (representative for $n = 4$ reslices from two different experiments). Scale bar = 20 μ m. Arrows point to CD206⁺ myeloid cells. (C) Representative staining of DAPI (blue), CD206 (red), CD4 (magenta), and Iba-1 (green) in EAE diseased animals ($n = 3$ mice [C57BL/6 or Cx3CR1.GFP] from two different experiments). The second panel demonstrates a probable blood vessel. Magnification of a slice view of CD206⁺ engulfing parenchymal (pc) and perivascular (pv) myeloid cell is shown in the third and fourth panel. Scale bars = 30 μ m in first and second panel and 20 μ m in the third and fourth panels.

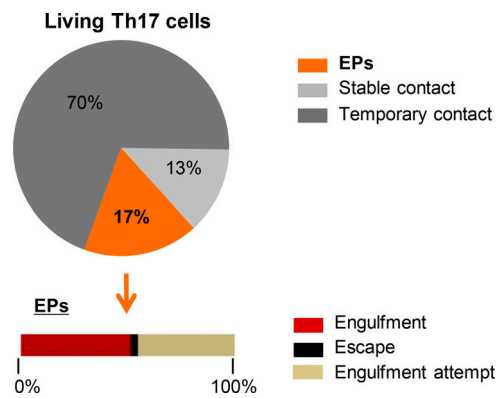


Figure S2. **Myeloid cells in organotypic hippocampal slices gained from CX3CR1.GFP^{+/-} mice show interactions similar to myeloid cells in organotypic hippocampal slices gained from CX3CR1.GFP^{+/+}.** 24-h co-cultures of organotypic hippocampal slices from CX3CR1.GFP^{+/-} pups with pathogenic B6.2D2.CFP.Th17 cells were stained with Image-iT LIVE Red Caspase-3 and -7 Detection Kit to identify apoptotic cells and imaged over a time period of 20 min with two-photon microscopy. The pie chart compares the distribution (%) of interaction modes between myeloid cells and viable 2D2.CFP.Th17 cells ($n = 4$ organotypic slices from two different experiments), and contingency bars reflect the respective distribution of engulfment, escape, and engulfment attempt. All interactions detectable in organotypic hippocampal slices from CX3CR1.GFP^{+/-} pups (Fig. 4 C) were observed.

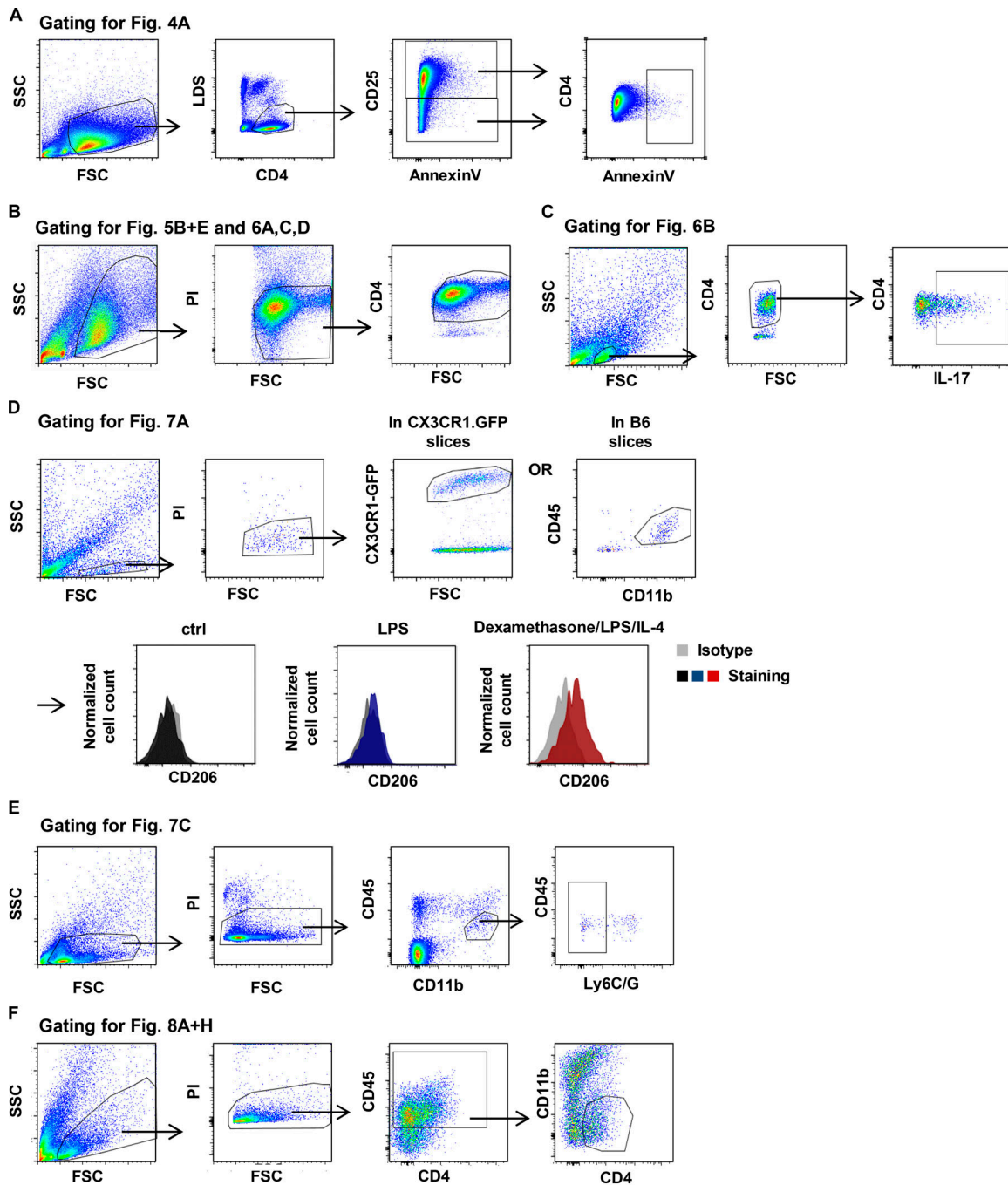


Figure S3. **Gating strategies.** (A–F) Gating strategies for all flow cytometric analyses used for the presented data are shown. The antibodies used are listed in the Materials and methods (experimental repeats in the respective figures). FSC, forward scatter; PI, propidium iodide; SSC, side scatter.

Video 1. **Surface-reconstructed intravital two-photon live imaging of an escaping T cell in vivo.** Related to Fig. 1. EAE was induced in CX3CR1^{GFP} (green CX3CR1⁺ cells) mice via the passive transfer of B6.2D2.RFP.Th17 cells (red). The engulfment and escape of a T cell was followed over time (10 min) in $n = 12$ mice from three different experiments. Shown here is the original GFP (myeloid cells) and RFP (Th17 cells) 3D image sequence (smoothened and 3D cropped to show a stable contact using Imaris) as well as the 3D-reconstructed version (Imaris). Time is shown in h/min/s.

Video 2. **Two-photon live imaging of Th17 cell–myeloid cell interactions ex vivo.** Related to Fig. 2. Organotypic hippocampal slices from CX3CR1^{GFP} pups were co-cultured with pathogenic B6.2D2.CFP.Th17 cells for 24 h and contacts were visualized in $n = 4$ organotypic slices from three different experiments. Shown here is the original CFP (Th17 cells, false colored here in red) and GFP (myeloid cells) 3D image sequence, smoothed and 3D cropped using Imaris. Time is shown in h/min/s/ms.

Video 3. **Two-photon live imaging of a temporary contact ex vivo.** Related to Fig. 2. Organotypic hippocampal slices from CX3CR1^{GFP} pups were co-cultured with pathogenic B6.2D2.RFP.Th17 cells for 24 h and contacts visualized over a time period of 10 min in $n = 4$ organotypic slices from three different experiments. Shown here is the original GFP (myeloid cells) and RFP (Th17 cells) 3D image sequence (smoothed and 3D cropped in Imaris to show a temporary contact) as well as the 3D-reconstructed version (Imaris; green is myeloid cells, and red is Th17 cells). Time is shown in h/min/s.

Video 4. **Two-photon live imaging of a stable contact ex vivo.** Related to Fig. 2. Organotypic hippocampal slices from CX3CR1^{GFP} pups were co-cultured with pathogenic B6.2D2.RFP.Th17 cells for 24 h and contacts visualized over a time period of 10 min in $n = 4$ organotypic slices from three different experiments. Shown here is the original GFP (myeloid cells) and RFP (Th17 cells) 3D image sequence (smoothed and 3D cropped to show a stable contact using Imaris) as well as the 3D-reconstructed version (Imaris). Time is shown in h/min/s.

Video 5. **Two-photon live imaging of a stable engulfment ex vivo.** Related to Fig. 2. Organotypic hippocampal slices from CX3CR1^{GFP} pups were co-cultured with pathogenic B6.2D2.RFP.Th17 cells for 24 h and contacts visualized over a time period of 10 min in $n = 4$ organotypic slices from three different experiments. Shown here is the original GFP (myeloid cells) and RFP (Th17 cells) 3D image sequence (smoothed and 3D cropped to show a stable engulfment using Imaris) as well as the 3D-reconstructed version (Imaris). Time is shown in h/min/s.

Video 6. **Two-photon live imaging of an escape following walk-through ex vivo.** Related to Fig. 2. Organotypic hippocampal slices from CX3CR1^{GFP} pups were co-cultured with pathogenic B6.2D2.RFP.Th17 cells for 24 h and contacts visualized over a time period of 10 min in $n = 4$ organotypic slices from three different experiments. Shown here is the original GFP (myeloid cells) and RFP (Th17 cells) 3D image sequence (smoothed and 3D cropped to show an escape following walkthrough in Imaris) as well as the 3D-reconstructed version (Imaris). Time is shown in h/min/s.

Video 7. **Two-photon live imaging of an engulfment attempt.** Related to Fig. 2. Organotypic hippocampal slices from CX3CR1^{GFP} pups were co-cultured with pathogenic B6.2D2.RFP.Th17 cells for 24 h and contacts visualized over a time period of 10 min in $n = 4$ organotypic slices from three different experiments. Shown here is the original GFP (myeloid cells) and RFP (Th17 cells) 3D image sequence (smoothed and 3D cropped to show engulfment attempts in two independent myeloid cells using Imaris) as well as the 3D-reconstructed version (Imaris). Time is shown in h/min/s.

Video 8. **Two-photon live imaging of a long-term engulfment.** Related to Fig. 3. Organotypic hippocampal slices from CX3CR1^{GFP} pups were co-cultured with pathogenic B6.2D2.CFP.Th17 cells for 24 h and contacts visualized in $n = 4$ co-cultures from three different experiments. Shown here is the original CFP (Th17 cells, false colored in red) and GFP (myeloid cells) 3D image sequence, smoothed and 3D cropped with Imaris to show a long-term engulfment. Time is shown in h/min/s.

Video 9. **Two-photon live imaging of a long-term escape.** Related to Fig. 3. Organotypic hippocampal slices from CX3CR1^{GFP} pups were co-cultured with pathogenic B6.2D2.CFP.Th17 cells for 24 h and contacts imaged in $n = 4$ co-cultures from three different experiments. Shown here is the original CFP (Th17 cells, false colored in red) and GFP (myeloid cells) 3D image sequence, smoothed and 3D cropped with Imaris to show a long-term escape. Time is shown in h/min/s.

Video 10. **In vivo dynamics of T cell–myeloid cell interactions during early and chronic disease.** EAE was induced in CX3CR1^{GFP} (green CX3CR1⁺ cells) mice via the passive transfer of B6.2D2.RFP.Th17 cells (red). Interactions between T cells and myeloid cells were visualized in mice exhibiting low or high clinical scores. Representative of $n = 9$ mice from two different experiments. Time is shown in h/min/s/ms.